Delft University of Technology
Faculty of Applied Sciences

Master Thesis Applied Physics
AP3902-MPT

A Unified Model to Predict Excited State Cyclicity of Nitrogen Vacancy Centres in Diamond

Author:
Otmar Ubbens (4579321)

Supervisor:
Prof. dr. ir. Ronald Hanson

Daily supervisor:
Ir. Kian van der Enden

June 22, 2022

Abstract

Crucial to the behaviour of a Nitrogen-Vacancy (NV) centre are its excited state cyclicities, determining the ability to perform high fidelity readout, spin-photon entanglement generation or fast spinpumping. This work presents a unified model to predict these excited state cyclicities over a wide range of strain, electric field, magnetic field and temperature, a useful tool for a model based predictive engineering approach towards the development of new NV qubits.

A set of measurements was performed to verify the prediction made by the model and improve the model over a wide range of perpendicular strain up to 7.5 GHz. An automated photon detection efficiency measurement was implemented, showing an average PSB photon detection efficiency of 2.8(3)% in the given setup. The cyclicities of the $|E_x\rangle$ and $|E_y\rangle$ excited states were measured over the given strain range for a single NV centre, showing a severe drop in cyclicity towards higher strain for both transition, a convergence of cyclicities towards zero strain, and a consistently higher cyclicity for $|E_x\rangle$ compared to $|E_y\rangle$, as predicted by the model. However, clear differences were discovered between predictions and measurements, with the recommendation to repeat the measurement at a lower sample temperature of 4 K where temperature mixing is negligible. A framework was developed to measure the excited state branching ratios into and out of the singlet states, and were measured for the $|E_{1,2}\rangle$ states, showing that significant singlet branching remains present at high strain. However, a broken optical device prevented accurate measurements.

Furthermore, an optimisation framework was developed, implemented and verified for a mirror coupling light out of a quantum frequency converter into a telecom fibre; one of the final steps towards an operationally autonomous NV quantum network node.

Contents

1 Introduction

With a long march up, quantum mechanics is aiming to move from a fundamental research topic towards a tool in an engineer's toolbox. One of the important tools will be the ability to transfer quantum information long distances: the quantum internet [1]. Similar to the classical internet allowing for bits to be moved between locations far apart, the quantum internet aims to do the same with quantum bits, or qubits, generating quantum entanglement between distant quantum computers. This has all the benefits of working with quantum states: from quantum key distribution to large-scale distributed quantum computing networks. A battle is ongoing between multiple types of quantum computers with their own strengths and weaknesses. One such platform, the Nitrogen Vacancy (NV) centre in diamond, is particularly suited to lead the path towards a quantum internet. This type of qubit interacts with light particles, photons, to control and share its information. These photons can then be captured into optical fibres, and sent to other NV centres to generate entanglement between them.

This work is performed in the context of the QLink Demonstrator project, a project which aims to set the next step towards a quantum future by providing the first elementary quantum network link at metropolitan distance: generating entanglement between two independent nodes in Delft and The Hague, using a midpoint in Rijswijk; see Figure 1.1. A critical innovation towards this goal is the use of quantum frequency converters (QFC), where the frequency of the NV centre's photons is transformed to the telecom frequency band for improved range, while keeping its quantum information. The core challenges in this project are centred around the indistinguishability of the photons coming from the NV centres, and around operational autonomy and long-term reliability of the two independent setups. This requires numerous automated calibrations, such as frequency, time and polarisation calibration of the photons, and position and charge calibration of the NV centres. One such calibration is implemented as part of this work: the calibration of the mirror coupling the light of the frequency-converted light into the fibre towards the midpoint.

Zooming in, it is crucial for entanglement generation to have good control over the qubits themselves. Particularly, reading out the state of the qubit, and generating a photon entangled with the state of the qubit are two of the most basic and critical operations. Focusing on reading out the state, this is performed by sending in a light pulse resonant with one the the NV centre's excited state transitions, to which the NV centre only responds by emitting a photon when in the correct ground state. The detection of a photon then tells us the qubit's state. However, the probability to actually detect an emitted photon is very low. Therefore, the emission process needs to be repeated many times to get a good chance to detect such a photon, and thus know the qubit's state. The ability to repeat the operation many times before the qubit state jumps away is called the cyclicity, and it is also crucial to generate good entanglement between the qubit's state and a photon sent out. This work presents a unified model to predict the NV centre's excited state cyclicities for different environmental variables, such as strain, electric field, magnetic field and temperature, and tries to verify this model by investigating the cyclicities when sweeping the strain. This is especially useful for a model based system engineering approach towards the development and fast characterisation and assessment of new NV qubits.

This work is structured as follows: firstly, the theory of the NV centre and the QLink demonstrator setup are presented in Chapters 2 and 3. Then, the QFC output mirror optimisation framework and results are discussed in Chapter 4. Next, the excited state cylicity model is presented in Chapter 5. The measurements to verify the model are explained in Chapter 6 and the corresponding results are presented in Chapter 7. Finally, the results are discussed in Chapter 8.

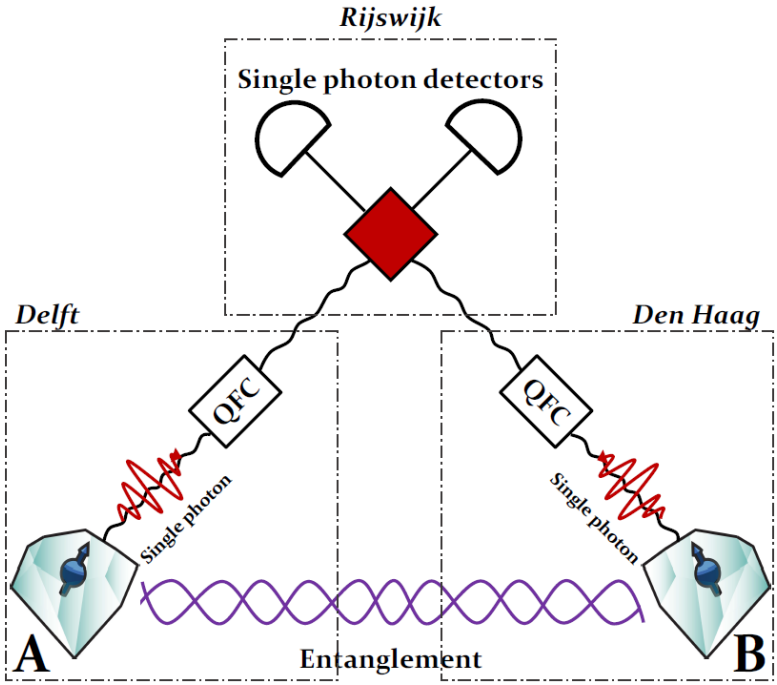

Figure 1.1: ***Schematic representation of the QLink demonstrator setup*** *to generate remote entanglement between two NV centers located in Delft and The Hague (Den Haag), mediated by a midpoint station located in Rijswijk. Light from the nodes is converted to the telecom waveband using Quantum Frequency Converters (QFC) to minimise photon loss. Image taken from [2].*

2 Theory

This theory section will first explain the working and control of NV centre qubits and how to transform them to telecom wavelength, and secondly explain the two protocols used to generate entanglement between two such qubits. The detailed theory relevant for the excited state cyclicity model is omitted from this section, and instead taken up in Chapter 5 presenting the cyclicity model itself.

2.1 NV centre

An NV centre is defined as a local defect in a diamond lattice, where two neighbouring carbon atoms have been replaced by a single nitrogen atom and a lattice vacancy. We are interested in the negative charge state of this centre (NV^-), in which the NV centre has six unbound electrons (two from the nitrogen atom, three from the carbon atoms neighbouring the vacancy, and one from the environment), which occupy orbitals with energy levels between the valence and conduction band of the diamond. The electrons form a spin-1 system, in which the system's ground state triplet ($^3A_2$) and excited state triplet (^3E) are of interest to us [3–6].

2.1.1 Energy levels

The ground state can be in one of three spin states, $m_s = -1, 0, 1$, with a zero-field splitting of $D_{gs} \approx 2.88\,\text{GHz}$ between $m_s = 0$ and $m_s = \pm 1$. In an aligned external magnetic field, the $m_s = \pm 1$ states get a further Zeeman splitting of $\gamma_e \approx 2.802\,\text{MHz/G}$. With this splitting, a qubit can be defined by taking $m_s = 0$ and one of $m_s = \pm 1$ as qubit states, defining $m_s = 0$ as $|0\rangle$, and one of $m_s = \pm 1$ as $|1\rangle$. The complete energy level diagram is shown in Figure 2.1.

The ground states can be optically excited to the excited ^3E state. This can be performed resonantly using a wavelength of $\lambda \approx 637\,\text{nm}$, or off-resonantly to a higher energy level, which in turn quickly decays to the ^3E state. This ^3E state will decay back to the ground state triplet either directly, via a phonon level, or via the singlet states. In the first two cases, respectively, either a photon is emitted with the exact resonant wavelength (Zero Phonon Line, ZPL) or with a larger wavelength (Phonon Side Band, PSB), both with a decay time of 12 ns. The singlet state decay occurs without emission of a visible photon, and on a longer timescale of around 400ns. Around 3% of visible decay is in the ZPL line, with the remaining 97% being PSB decay [7].

The excited states themselves are split into multiple levels by spin-spin and spin-orbit interactions, and are sensitive to strain and electric fields. There are two excited levels with spin $m_s = 0$, $E_{x,y}$, and four with spin $m_s = \pm 1$, $E_{1,2}, A_{1,2}$, each of which with different energies and strain/electric field dependencies. Optical transitions between the ground and excited states are only allowed for the same value of m_s, and each transition can be addressed individually at cryogenic temperatures. ZPL and PSB decay maintain the value of m_s, while it is randomised for singlet decay, meaning a chance to get state randomisation after excitation. The $m_s = \pm 1$ states are more likely to decay via the singlet path, with a large probability to end up in the $m_s = 0$ ground state. A more detailed theory of excited state decay is presented in Chapter 5.

2.1.2 Qubit readout and control

The energy levels and transitions can be applied to selectively initialise and read out the $|0\rangle$ and $|1\rangle$ states defined earlier. Choosing one of the transitions $E_{x,y}$ and $A_{1,2}/E_{1,2}$ for $|0\rangle$ and $|1\rangle$, respectively, allows for selective excitation of only one of the two spin states. Driving one of these transitions will therefore only generate photons if the NV is in the corresponding spin state, providing a way to read out this state. Particularly the $|0\rangle \rightarrow E_{x,y}$ transitions yield high photon counts due to their high cyclicity, making them ideal to read out the qubit spin state. Careful tuning of the excitation pulse even allows for single-shot readout (SSRO) with a fidelity up to around 95% [2, 6, 8].

Conversely, pumping the $|1\rangle \rightarrow A_{1,2}/E_{1,2}$ transitions for longer periods of time yields a large probability for the final state to end up in $|0\rangle$ through singlet decay, making it a good way to initialise ('pump') the state to $|0\rangle$ with fidelities up to $99.7 \pm 0.1\%$ [7]. Hence, the $|0\rangle \rightarrow E_{x,y}$ and $|1\rangle \rightarrow A_{1,2}/E_{1,2}$ transitions are called the Readout (RO) and Spin Pump (SP) transitions, respectively. The simplified energy level diagram is shown in Figure 2.2.

Further control of the spin state can be achieved through Rabi driving of the $|0\rangle \leftrightarrow |1\rangle$ transition: providing a microwave signal with the precise frequency of the transition ($\sim 2.88\,\text{GHz}$) gives a stable magnetic field in

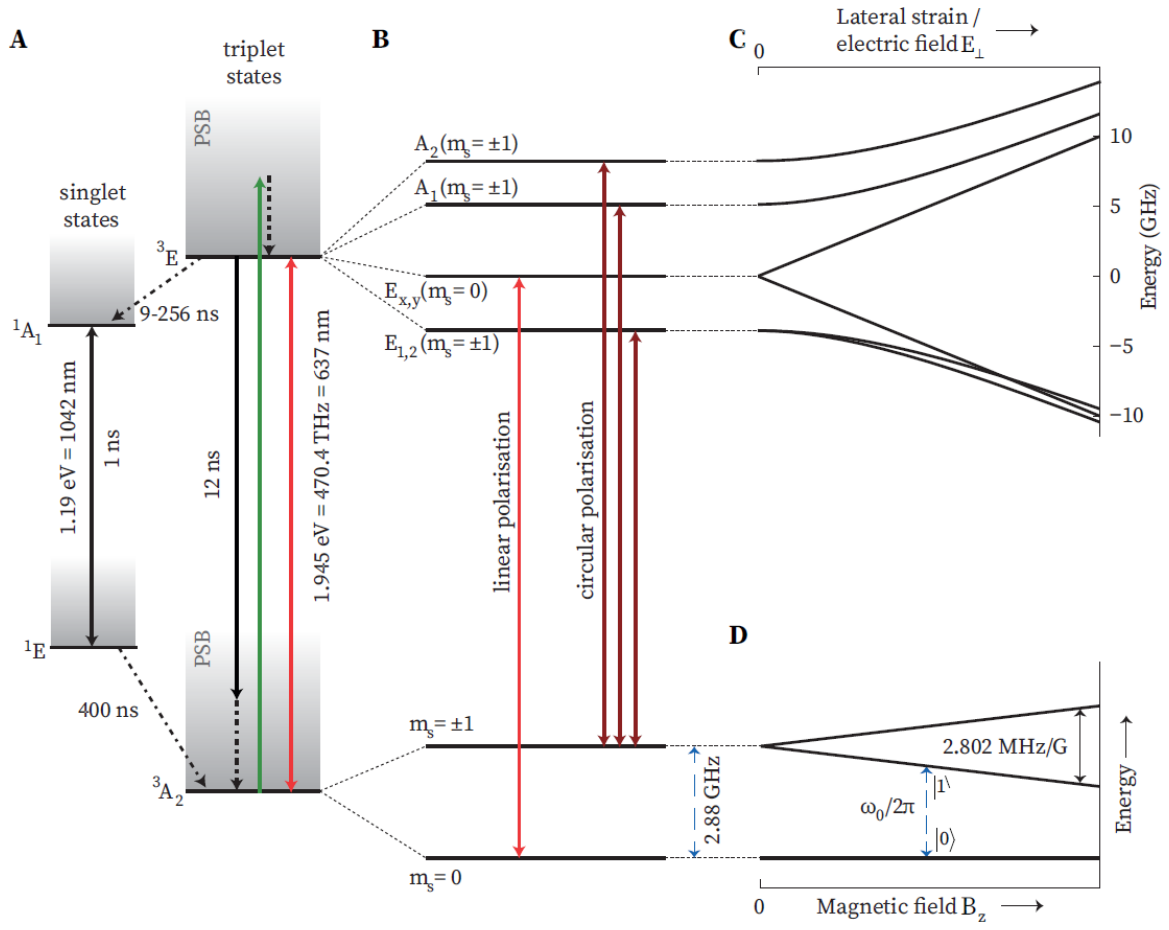

Figure 2.1: ***Electronic level structure of a negatively charged NV centre.*** *(A) Resonant (ZPL, bright red arrow) and off-resonant (PSB, green and black arrow) excitation and emission between the spin triplet ground state $^3A_2$ and excited state ^3E. The excited state can also decay via the singlet states, with the emission of photons with frequencies far from the excitation frequency. (B) The splitting of energy levels at cryogenic temperatures, without external magnetic field. At cryogenic temperatures, the $m_s = 0$ and $m_s = \pm 1$ states can be excited separately, represented by the bright red and dark red arrows, respectively. (C) Energy splitting of the energy levels of the excited triplet state due to lateral strain or an external electric field. (D) Lifting of the $m_s = \pm 1$ energy level degeneracy by application of a magnetic field applied along the NV main axis. This allows to define a qubit within the ground state triplet. Image taken from [8].*

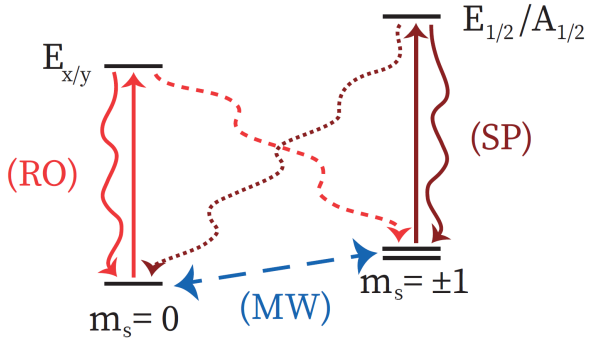

Figure 2.2: ***Simplified schematic of the electronic energy levels*** *showing transitions which can be driven by Readout (RO) and Spin Pump (SP) lasers, as well as Microwave (MW) radiation. The dotted lines imply lower probability transitions.*

the rotating frame, causing a rotation around an axis in the x/y plane. This angular velocity is dependent on the signal strength and detuning. Well-timed microwave pulses can accurately rotate the state, with of particular interest being π-pulses (flipping $|0\rangle \leftrightarrow |1\rangle$) and $\pi/2$-pulses (rotating $|0\rangle$ and $|1\rangle$ to equal superposition states).

The transitions described in this section only hold when the NV centre is in its negative state, i.e. NV^-, and when the RO and SP laser frequencies are aligned with their respective transitions. With time, however, the additional electron may escape, or the transitions move through shifting charges in the environment. To restore the NV to its negative charge and keep the laser on resonance, charge-resonance (CR) checks are performed intermittently throughout experiments. A thorough description of CR checking can be found in [8]. The CR check incurs overhead in performing measurements, as a CR check round can take several ms of time.

2.1.3 Frequency down-conversion

One of the major hurdles for long-range quantum communication through fibres is attenuation of the signal. The 637 nm ZPL light sent out by NV centres has a large attenuation of 8 dB/km [9], which makes sending single photons over the envisioned 10+ kilometres in the QLink Demonstrator project completely infeasible [9]. The key to solving this issue is to down-convert the ZPL photons coming from the NVs to a more ideal wavelength for fibre transmission, while maintaining the quantum properties of the photons themselves; a process commonly referred to as quantum frequency conversion (QFC). Specifically, the ZPL photons are converted to 1588 nm in the L-telecommunication waveband, where an attenuation < 0.2 dB/km can be achieved [10].

The frequency down-conversion is achieved by frequency-difference generation (DFG) in a non-linear PPLN crystal, pumped by an strong laser at 1064 nm. That is, under the right phase-matching conditions, the incoming 637 nm photon brings the system to a higher energy state, from which the pump light stimulates the emission of two photons: a 1064 nm photon through stimulated emission, and a second photon to maintain conservation of energy and momentum,

$$\frac{1}{\lambda_{NV}} = \frac{1}{\lambda_{pump}} + \frac{1}{\lambda_{tel}} \qquad \vec{k}_{NV} = \vec{k}_{pump} + \vec{k}_{tel}, \tag{2.1}$$

where λ denotes the wavelength and $\vec{k}$ the wavevector of the light. Computing λ_t shows that the telecom photon indeed has a wavelength of 1588 nm. Importantly, it has been shown that the 1588 nm photons maintain the properties of the incoming 637 nm ZPL photons [11], and can be filtered from the other light and coupled into a fibre toward its destination [10].

Frequency conversion has the additional benefit that outgoing telecom light can be tuned by changing the pump laser frequency. This way, two NVs can interfere their ZPL photons without the need to have the same frequency, meaning that DC Stark tuning of the node frequencies can be omitted [10].

2.2 Entanglement generation

A major intermediate milestone of the QLink Demonstrator project is to show entanglement between two independent NV centre qubits over a metropolitan distance. In this section, two entanglement generation methods

are discussed: single click [12] and Barrett-Kok [13].

A core concept for both schemes is spin-photon entanglement, which is the process of entangling the state of a photon to that of the state of a qubit. In the case of NV centres, it can be created by exciting the spin state exactly once using a very short ($\sim$ 1 ns) RO laser pulse, often called an optical pi-pulse. Ideally, exactly one photon is emitted for the $|0\rangle$ state, and none for the $|1\rangle$ state. When the NV centre is initially in a superposition state, this process creates an entangled state of $|0\rangle$ and a photon, or $|1\rangle$ and no photon. It is important to note that this only occurs when a ZPL photon is emitted. In case of PSB photons, the state is effectively measured by the environment, and the superposition state collapses. To avoid unwanted states, the PSB photons can be filtered out and detected. In case of PSB detection, the protocol is restarted.

Both entanglement generation schemes apply spin-photon entanglement similarly. In the setups, the optical outputs of two NV centres are connected to the two inputs of an equal beamsplitter (BS), and the two outputs of the beamsplitter are each connected to a Single Photon Detector (SPD). The NV centres are brought in a superposition of $|0\rangle$ and $|1\rangle$, and spin-photon entanglement is generated. The photons from both NV centres are then interfered on the beamsplitter, creating entanglement between the NV centres depending on SPD output.

The effect of the beamsplitter on indistinguishable photons can be described in Fock space using creation operators. Defining the inputs as $1, 2$ and outputs as A, B, the input creation operators are transformed as

$$a^\dagger_{1/2} = \frac{1}{\sqrt{2}} \left(a^\dagger_A \pm a^\dagger_B \right). \tag{2.2}$$

The effect on the possible scenarios of photons incident on the beamsplitter then reads

$$\begin{aligned} |0_1\, 0_2\rangle &= |0_A\, 0_B\rangle\,, \\ |1_1\, 0_2\rangle &= \frac{1}{\sqrt{2}} \left(|1_A\, 0_B\rangle + |0_A\, 1_B\rangle \right), \\ |0_1\, 1_2\rangle &= \frac{1}{\sqrt{2}} \left(|1_A\, 0_B\rangle - |0_A\, 1_B\rangle \right), \\ |1_1\, 1_2\rangle &= \frac{1}{\sqrt{2}} \left(|2_A\, 0_B\rangle - |0_A\, 2_B\rangle \right), \end{aligned} \tag{2.3}$$

where the phases of the $|1_A\, 1_B\rangle$ contributions of the last scenario cancel each other out, known as the Hong-Ou-Mandel (HOM) effect [14].

To avoid naming confusion between spins and photons, the NV spin states are defined as $|0\rangle \equiv |\uparrow\rangle$ and $|1\rangle \equiv |\downarrow\rangle$ in the following sections, while numbers are used for the photonic states.

2.2.1 Single click

To start the single click procedure, both NV centres are rotated to the state

$$|\uparrow\rangle \rightarrow \sqrt{\alpha}\, |\uparrow\rangle + \sqrt{1-\alpha}\, |\downarrow\rangle\,, \tag{2.4}$$

for some small value of α. This value determines a balance between entanglement generation efficiency and fidelity. Spin-photon entanglement on the states then gives

$$\sqrt{\alpha}\, |\uparrow\rangle + \sqrt{1-\alpha}\, |\downarrow\rangle \rightarrow \sqrt{\alpha}\, |\uparrow, 1\rangle + \sqrt{1-\alpha}\, |\downarrow, 0\rangle\,. \tag{2.5}$$

These photons are now sent to the beam splitter. Right before the beamsplitter, the combined state of both NV centres and photons reads

$$\begin{aligned} &\left(\sqrt{\alpha}\, |\uparrow, 1\rangle_1 + e^{i\varphi} \sqrt{1-\alpha}\, |\downarrow, 0\rangle_1 \right) \otimes \left(\sqrt{\alpha}\, |\uparrow, 1\rangle_2 + \sqrt{1-\alpha}\, |\downarrow, 0\rangle_2 \right) \\ &= \alpha\, |\uparrow_1 \uparrow_2\rangle\, |1_1 1_2\rangle + \sqrt{\alpha - \alpha^2} \Big(|\uparrow_1 \downarrow_2\rangle\, |1_1 0_2\rangle + e^{i\varphi}\, |\downarrow_1 \uparrow_2\rangle\, |0_1 1_2\rangle \Big) + e^{i\varphi} (1-\alpha)\, |\downarrow_1 \downarrow_2\rangle\, |0_1 0_2\rangle\,, \end{aligned} \tag{2.6}$$

where φ is a possible phase difference between the photons. The photons are then interfered on the beamsplitter according to Equation 2.3, yielding the combined state

$$\begin{aligned}
&(\alpha/\sqrt{2})\,|\uparrow_1\uparrow_2\rangle\,(|2_A\,0_B\rangle - |0_A\,2_B\rangle)\\
&+\sqrt{(\alpha-\alpha^2)/2}\,\big(|\uparrow_1\downarrow_2\rangle + e^{i\varphi}\,|\downarrow_1\uparrow_2\rangle\big)\,|1_A\,0_B\rangle\\
&+\sqrt{(\alpha-\alpha^2)/2}\,\big(|\uparrow_1\downarrow_2\rangle - e^{i\varphi}\,|\downarrow_1\uparrow_2\rangle\big)\,|0_A\,1_B\rangle\\
&+e^{i\varphi}(1-\alpha)\,|\downarrow_1\downarrow_2\rangle\,|0_A0_B\rangle\,,
\end{aligned} \tag{2.7}$$

after a slight rewrite. We are only interested in situations where photons are detected, so we can select on detecting non-$|0_A0_B\rangle$ results, with a probability proportional to $\sqrt{\alpha}$. Furthermore, SPDs are generally not photon-number resolving, meaning that detecting 1 or 2 photons appears identical. Defining 1^+ as 1 or 2 we can then rewrite the total detectable state (without $|0_A0_B\rangle$ contribution) as

$$\begin{aligned}
\frac{1}{\sqrt{4-2\alpha}}\Big\{\,&|1_A^+\,0_B\rangle\,\Big[\sqrt{1-\alpha}\big(\,|\uparrow_1\downarrow_2\rangle + e^{i\varphi}\,|\downarrow_1\uparrow_2\rangle\,\big) + \sqrt{\alpha}\,|\uparrow_1\uparrow_2\rangle\Big]\\
&+\;|0_A\,1_B^+\rangle\,\Big[\sqrt{1-\alpha}\big(\,|\uparrow_1\downarrow_2\rangle - e^{i\varphi}\,|\downarrow_1\uparrow_2\rangle\,\big) - \sqrt{\alpha}\,|\uparrow_1\uparrow_2\rangle\Big]\Big\}.
\end{aligned} \tag{2.8}$$

Depending on which detector clicks, we thus get the final state

$$\propto \sqrt{1-\alpha}\Big(\,|\uparrow_1\downarrow_2\rangle \pm e^{i\varphi}\,|\downarrow_1\uparrow_2\rangle\,\Big) \pm \sqrt{\alpha}\,|\uparrow_1\uparrow_2\rangle\,. \tag{2.9}$$

For $\alpha \to 0$, this gives better-and-better approximation of the maximally entangled states

$$|\Phi^{\pm}(\varphi)\rangle \equiv \frac{1}{\sqrt{2}}\Big(\,|\uparrow_1\downarrow_2\rangle \pm e^{i\varphi}\,|\downarrow_1\uparrow_2\rangle\,\Big). \tag{2.10}$$

Hence, we find a near-maximally entangled state with a fidelity proportional to $1-\alpha$, and a success rate proportional to α. It should be noted that the result is phase dependent; an unknown phase term φ is detrimental to quantum experiments.

2.2.2 Barrett-Kok

The Barrett-Kok scheme is similar to single click, with the main difference that Barrett-Kok applies two spin-photon entanglement steps to get theoretically ideal final states and make the procedure phase independent. In the Barrett-Kok procedure, the NV states are first initialised to an equal superposition (i.e. $\alpha = 0.5$). Like single click, spin-photon entanglement is performed on the states, but now the state is additionally flipped and a second spin-photon entanglement step is performed. This yields a superposition of either an early or late photon, entangled with the spin state,

$$\begin{aligned}
&\frac{1}{\sqrt{2}}\Big(\,|\uparrow\rangle + |\downarrow\rangle\,\Big)\\
&\xrightarrow{\text{sp-ph}}\ \frac{1}{\sqrt{2}}\Big(\,|\uparrow;E\rangle + |\downarrow;0\rangle\,\Big)\\
&\xrightarrow{\text{flip}}\ \frac{1}{\sqrt{2}}\Big(\,|\downarrow;E\rangle + |\uparrow;0\rangle\,\Big)\\
&\xrightarrow{\text{sp-ph}}\ \frac{1}{\sqrt{2}}\Big(\,|\downarrow;E\rangle + |\uparrow;L\rangle\,\Big),
\end{aligned} \tag{2.11}$$

where we denote a single early and late photon as $|E\rangle$ and $|L\rangle$, respectively. Right before the beamsplitter, the combined state now becomes

$$\begin{aligned}
&\frac{1}{2}\Big(e^{i\varphi_E}\,|\downarrow_1;E_1\rangle + e^{i\varphi_L}\,|\uparrow_1;L_1\rangle\,\Big)\otimes\Big(\,|\downarrow_2;E_2\rangle + |\uparrow_2;L_2\rangle\,\Big)\\
&= \frac{e^{i\varphi_E}}{2}\Big(\,|\downarrow_1\downarrow_2\rangle\,|E_1E_2\rangle + |\downarrow_1\uparrow_2\rangle\,|E_1L_2\rangle + e^{i\Delta\varphi}\,|\uparrow_1\downarrow_2\rangle\,|L_1E_2\rangle + e^{i\Delta\varphi}\,|\uparrow_1\uparrow_2\rangle\,|L_1L_2\rangle\,\Big),
\end{aligned} \tag{2.12}$$

for early and late photons with a phase difference of φ_E and φ_L, respectively, and a relative phase difference of $\Delta\varphi \equiv \varphi_L - \varphi_E$. The effect of the beamsplitter on the photons now reads, ignoring the global phase term

$$\begin{aligned}\frac{1}{2\sqrt{2}}\Bigg[& |{\downarrow_1}{\downarrow_2}\rangle \Big(|2_A 0_B\rangle_E - |0_A 2_B\rangle_E \Big) |0_A 0_B\rangle_L \\ & + \frac{1}{\sqrt{2}} |{\downarrow_1}{\uparrow_2}\rangle \Big(|1_A 0_B\rangle_E + |0_A 1_B\rangle_E \Big) \Big(|1_A 0_B\rangle_L - |0_A 1_B\rangle_L \Big) \\ & + \frac{e^{i\Delta\varphi}}{\sqrt{2}} |{\uparrow_1}{\downarrow_2}\rangle \Big(|1_A 0_B\rangle_E - |0_A 1_B\rangle_E \Big) \Big(|1_A 0_B\rangle_L + |0_A 1_B\rangle_L \Big) \\ & + e^{i\Delta\varphi} |{\uparrow_1}{\uparrow_2}\rangle |0_A 0_B\rangle_E \Big(|2_A 0_B\rangle_L - |0_A 2_B\rangle_L \Big) \Big) \Bigg],\end{aligned} \tag{2.13}$$

where only two early or two late photons can show HOM interference. This time, selection is performed on detecting both an early and a late detector click, meaning that only the middle lines are kept into consideration. Then, only detector syndromes of $|1_A 0_B\rangle$ and $|0_A 1_B\rangle$ remain, i.e. a click in either detector A or B. The complete syndrome then becomes one early and one late click, both times in either detector A or B. Rescaling and defining $|A\rangle \equiv |1_A 0_B\rangle$, $|B\rangle \equiv |0_A 1_B\rangle$, and $|X_E Y_L\rangle \equiv |X\rangle_E |Y\rangle_L$ ($X, Y \in \{A, B\}$) then yields the final possible states

$$\begin{aligned}& \frac{1}{2\sqrt{2}}\Bigg[|{\downarrow_1}{\uparrow_2}\rangle \Big(|A\rangle_E + |B\rangle_E \Big) \Big(|A\rangle_L - |B\rangle_L \Big) \\ & \qquad + e^{i\Delta\varphi} |{\uparrow_1}{\downarrow_2}\rangle \Big(|A\rangle_E - |B\rangle_E \Big) \Big(|A\rangle_L + |B\rangle_L \Big) \Bigg] \\ = & \frac{1}{2\sqrt{2}}\Bigg[\Big(|A_E A_L\rangle - |B_E B_L\rangle \Big) \Big(|{\downarrow_1}{\uparrow_2}\rangle + e^{i\Delta\varphi} |{\uparrow_1}{\downarrow_2}\rangle \Big) \\ & \qquad + \Big(|A_E B_L\rangle - |B_E A_L\rangle \Big) \Big(|{\downarrow_1}{\uparrow_2}\rangle - e^{i\Delta\varphi} |{\uparrow_1}{\downarrow_2}\rangle \Big) \Bigg].\end{aligned} \tag{2.14}$$

Measuring the early and late clicks gives one of four possible A/B syndromes; depending on this syndrome we get the maximally entangled spin state

$$\frac{1}{\sqrt{2}} \Big(|{\downarrow_1}{\uparrow_2}\rangle \pm e^{i\Delta\varphi} |{\uparrow_1}{\downarrow_2}\rangle \Big), \tag{2.15}$$

where the sign depends on finding the two clicks in the same detector (+) or different detectors (−). If the phase difference between the photons stays constant within the timeframe of the two pulses, then $\Delta\varphi = 0$, which yields a maximally entangled Bell state

$$|\Phi^{\pm}\rangle = \frac{1}{\sqrt{2}} \Big(|{\downarrow_1}{\uparrow_2}\rangle \pm |{\uparrow_1}{\downarrow_2}\rangle \Big). \tag{2.16}$$

This final state therefore, theoretically, has no error, and is phase-independent (if the phase difference is constant), making it more robust than single click. The limitation of Barrett-Kok is the entanglement generation rate. The catch is that two photons need to be received by the detectors, as opposed to one for single-click. This makes the success rate of Barrett-Kok scale quadratically with photon survival probability, as opposed to linearly for single click. In practical scenarios, this probability can be exceedingly low, making Barrett-Kok a far slower scheme.

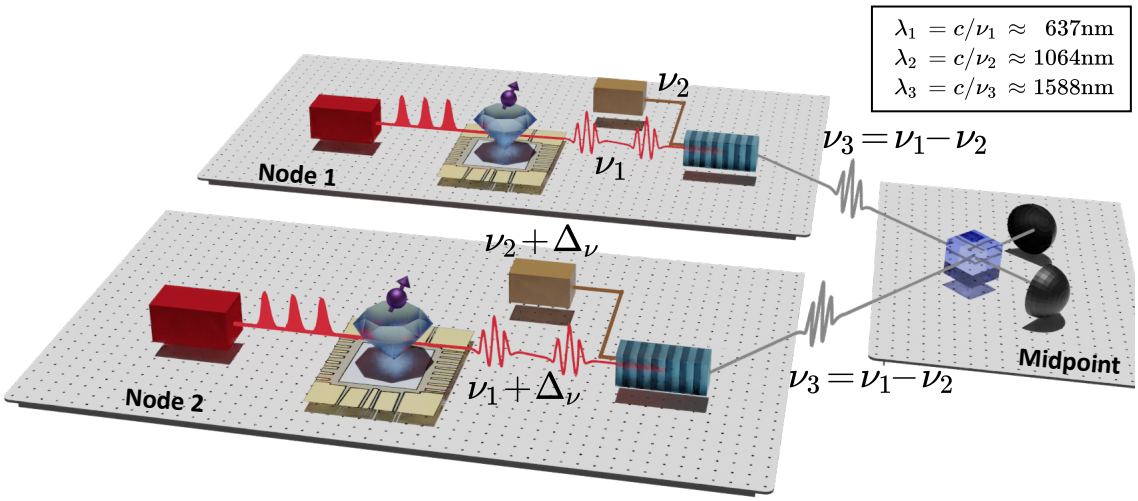

Figure 3.1: ***Complete QLink Demonstrator experimental setup.*** *The Nodes contain NV centre control and frequency down-conversion of ZPL photons to telecom wavelength. The nodes are designed to indepently operate kilometres apart, and to only communicate with the midpoint over deployed fibre. Image taken from [15].*

3 Experimental setup

In this section the current experimental setup of the QLink Demonstrator project is described. First, the Nodes containing the NV centres are discussed, including the physical samples in which the NV centres are embedded, the optical addressing of these NV centres, and the collection of their emission. Next, the implementation of the NV ZPL emission conversion to telecom is described, finally followed by a description of the telecom photon frequency locks to the midpoint's filtering. A diagram detailing the full experimental setup of the QLink Demonstrator project is shown in Figure 3.1.

3.1 Node setup

The nodes in the QLink Demonstrator project are responsible for the control of a single NV centre, perform spin-photon entanglement, and send out the ZPL photons with high fidelity. This section will describe the sample containing the NV centre, the optical addressing of this NV centre, and finally the collection of its ZPL photons.

3.1.1 Sample

A type IIa diamond, grown using chemical vapor deposition and cut in the $\langle 111 \rangle$ direction, is used as substrate. This diamond contains naturally occurring NV centres, from which ones in the 111 direction are chosen, such that the E_x and E_y fields are aligned orthogonally to the diamond surface. Around promising NV centres, a hemispherical solid immersion lense (SIL) is milled and an anti-reflection (AR) coating applied, to achieve improved optical addressing. A stripline is added to the diamond surface and two gates are added to each NV, such that, respectively, microwave (MW) fields and constant potentials can be applied to the NV centres, for qubit rotations and DC Stark tuning. Detailed explanations of these processes and features are described in [5, 6, 8, 16, 17].

The diamond sample is placed on a cold finger inside a closed-loop cryostat to cool the sample to 4K, and a permanent magnet is mounted behind the sample to split each NV's $|\pm 1\rangle$ levels. Focused on the sample is an objective, embedded within a vacuum chamber mounted to the cryostat. The objective can be moved in three dimensions using piezo steppers to allow focusing on the sample, and a window in the vacuum chamber allows for optical access to the objective. To optically inspect the sample, it can be viewed by flipping a mirror to a camera into the free-space optical path.

3.1.2 Optical addressing

In order to control the NV centre, the different transitions described in Section 2.1 need to be able to be driven. To this end, each node contains four lasers: two 637 nm lasers to drive the readout and spinpump transitions,

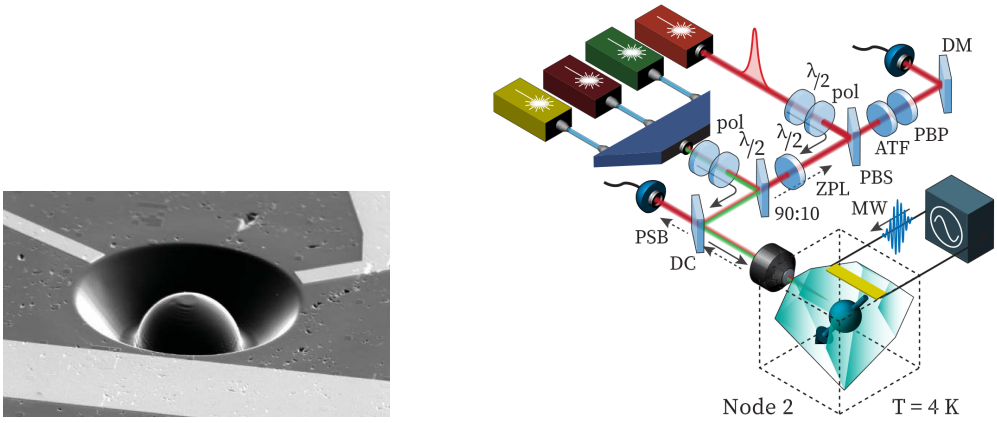

(a) (b)

Figure 3.2: ***(a) Solid immersion lens*** *as used in the setup. Image taken from [16],* ***(b) Schematic of the free-space optics in a node****, prior to frequency down-conversion. Solid arrows show the path light from the different lasers takes toward the sample, coupled into the main optical path by a 90:10 beamsampler or a polarising beamsplitter (PBS). From left to right these laser are the yellow, spinpump, green and readout lasers. Polarisers (pol) and half-waveplates (λ/2) ensure that the light arrives in the correct polarisation at the NV centre. Dashed arrows show the paths followed by light coming from the NV centre. The light is first split into two paths by a dichroic mirror (DC) of which the PSB path directly couples into an APD. The ZPL photons are filtered by the PBS (see Section 3.1.4), an angle tunable filter (ATF) and a polarising band-pass filter (PBP). The wavefront of the ZPL photons is corrected by a deformable mirror (DM), before before being coupled into fiber toward the QFC. Image taken from [8]. Not shown are the two motorised mirrors used for automated calibration of ZPL fibre incoupling, and neither is the path of the phase light; see Figure 3.1.*

a 515 nm green laser to off-resonantly perform charge resets, and a 575 nm yellow laser to resonantly perform charge resets. An additional frequency-shifted split-off from the readout laser, called the phase light, is used for the midpoint frequency lock, and will be discussed Section 3.3. See Figure 3.1 for details.

All lasers need to be able to excite/address the NV centre, for which their outputs need to be aligned onto the objective. To this end, the light of the spin pump, green and yellow lasers is combined in a colour combiner and fed into the optical path via the 10% arm of a 90:10 beam sampler. This power loss is a consideration to maximise the transmission of NV photons through the sampler. The readout light, meanwhile, is added to the optical path through a polarising beam splitter (PBS), the details of which are discussed in Section 3.1.4.

Both the frequencies and powers of the laser require calibrations to allow for accurate NV control. The frequencies are measured and locked using a wavemeter, fed by splitoffs of the light. Meanwhile, the power of each laser is modulated by an acousto-optical moduator (AOM). Moreover, the RO laser is modulated by a second AOM and an electro-optical modulator (EOM), such that it can attain the necessary attenuation and switching speed for optical pi-pulses. The control and timing of the AOMs and EOM is performed by the combination of an ADwin realtime processor and a 2.4GHz arbitrary waveform generator (AWG), synchronised within and between the nodes by a GPS disciplined heartbeat.

3.1.3 Collecting NV emission

Since the algorithms performed by the nodes and midpoint require transmission and detection of single photons, the setup is optimised to minimise the losses and noise in each node's ZPL path. Starting from the NV, the PSB photons are immediately split off and measured, while the ZPL photons are filtered from the other excitation light and coupled into fibre toward the QFC. See Figure 3.2b for details. Not shown are the two motorised mirrors tuning the ZPL fibre incoupling. Furthermore, the phase light is also coupled into the ZPL output by reflecting the phase light off the PBS, see Figure 3.1.

3.1.4 Excitation and detection polarisation

Since the frequency of the readout laser and the ZPL photons is identical, they cannot simply be split by their frequency. Instead, the light can only be split by polarisation, which is achieved by cross-polarisation rejection.

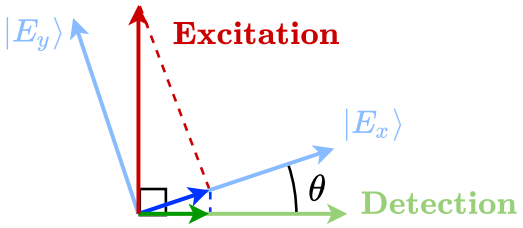

Figure 3.3: ***Polarisations of the excitation light and NV transitions*** *as projected onto the PBS. The chosen transition E_x is rotated such that it makes a small angle θ to the detection axis, resulting in a small fraction $\sin(\theta)$ of readout light exciting the transition, while a large fraction $\cos(\theta)$ of emitted ZPL light is transmitted through the PBS.*

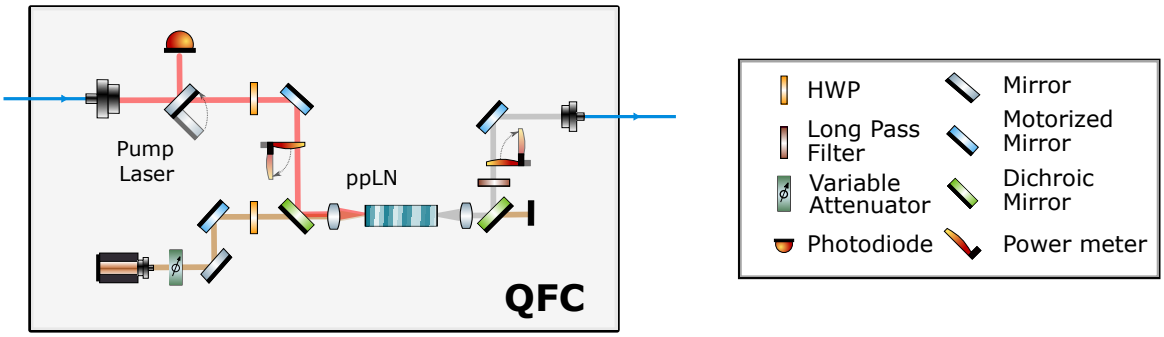

Figure 3.4: ***Optical setup for the quantum frequency conversion*** *as implemented on the nodes. The blue line on the left is the incoming ZPL fibre, and the blue line on the right is the outgoing telecom light. A mirror to an APD can be flipped in at the ZPL input to optimise ZPL incoupling. Similarly, a PM can be flipped into the QFC's output path to optimise ppLN incoupling of ZPL and pump light. The motorised mirrors for this purpose can be addressed remotely.*

The excitation light is polarised orthogonally to the transmission polarisation of the PBS, such that reflected readout light is split off from the ZPL path. Ideally, the NV transition's polarisation would be rotated such that it is maximally transmitted through the PBS for maximum signal. However, in this case, the excitation light is precisely orthogonal to the transition, meaning that no excitation will take place. The solution is to rotate the light from the NV centre by a small angle θ, such that an approximately linear fraction of the readout light can excite the NV centre, while only an approximately quadratic loss is achieved in the transmission of the ZPL photons; see Figure 3.3. To optimise for ZPL transmission, the angle θ can be decreased until the excitation laser is barely able to excite the transition. A typical angle used in the setup is $\theta = 24.5°$.

3.2 Frequency Conversion

As explained in Section 2.1.3, the ZPL photons coming from the nodes are converted to telecom wavelength before being sent to the midpoint. This difference frequency generation process is stimulated in a ppLN crystal by a 100 mW pump laser, the setup for which is shown in Figure 3.4. For the frequency conversion process to be successful at single photon regimes, a high conversion efficiency and low noise floor are critical.

Unfortunately, with DFG, the higher frequency of the pump light creates significant noise at larger wavelengths spontaneous, from parametric down-conversion of the pump light of imperfections in the nonlinear crystal. Only filtering out the 1064 nm light itself is therefore insufficient, meaning that strict filtering around the telecom frequency is critical. Firstly, the 1064 nm pump light is filtered out within the QFC, right after the ppLN crystal. Secondly, at the midpoint, the telecom photons are filtered more strictly by a set of two fibre Bragg gratings (FBGs). The most narrow of these two filters, hereafter called the ultra-narrow filter (UNF), has a FWHM of just 50 MHz. This is in the same order as the lifetime limited linewidth of the ZPL photons, to maximally limit the transmission of SPDC noise. The active feedback process to maintain indistinguishable transmission of telecom photons through the UNFs of both nodes is described in Section 3.3. This feedback system requires the 400 MHz detuned phase light introduced in Section 3.1.2, which is also converted to telecom frequency by the QFC and sent to the midpoint.

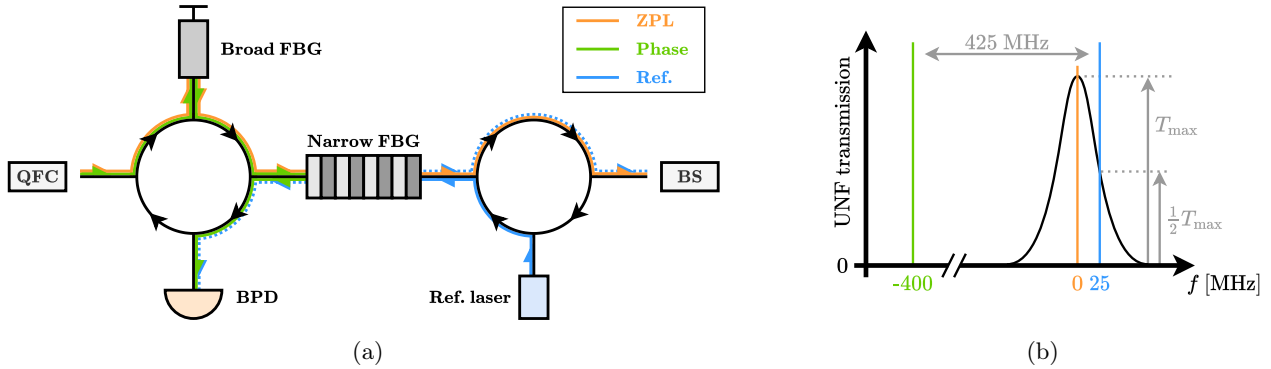

(a) (b)

Figure 3.5: ***(a) Implementation of filtering at the midpoint.*** *The broad FBG roughly filters out noise by only reflecting light within a range of 1 GHz around the desired telecom frequency. The narrow FBG (UNF), meanwhile, strictly filters out ZPL photons by only transmitting light within a range of* 50 MHz*, close to the lifetime limited linewidth of the ZPL photons. The two circles in the diagram represent optical circulators. Incoming ZPL photons are reflected off the broad FBG, travel through the UNF, and continue on to the beamsplitter (BS). Incoming phase light also reflects off the broad FBG, but is reflected by the UNF to land on the balanced photodiode (BPD). The reference (ref) light partially travels through the UNF, also to land on the BPD. The remainder is reflected off the UNF and travels to the BM and SNSPDs. The reference light, orders of magnitude brighter than the phase light, creates a DC signal at the BPD, while interference between the phase and reference light creates a high-frequency beat on top of the DC signal.* ***(b) Laser frequencies relative to the UNF transmission peak.*** *The UNF has a FWHM of* 50 MHz*, and is locked to the reference laser by adjusting its transmission to half of the maximum T_{max}, giving the reference light a* 25 MHz *detuning from the transmission peak (chosen at the higher side). ZPL light transmission through the UNF is optimised by locking the frequency offset between the reference light and phase light (offset* -400 MHz *from ZPL light) to* 425 MHz*. For practical purposes, this* 425 MHz *beat is mixed down to* 100 MHz *for locking.*

To maximise conversion efficiency, the pump and signal light is strongly confined by a waveguide etched into the ppLN crystal, and an anti-reflection coating is applied to both ends of the crystal. The internal conversion efficiency of the ppLN crystal is dependent on pump power, and reaches a peak efficiency of $\sim 60\%$ at a pump power of $\sim$100 mW. The efficiency is reduced to $\sim 10\%$ by the strict filtering, and by crystal and fibre incoupling. Noise at the given pump power reaches $\sim$100 Hz [8, 15].

To allow for correction of drifts, remotely operable motorised mirrors are included in the QFC's free space optics: two mirrors to keep the pump and ZPL light aligned with the crystal, and one to efficiently couple the telecom photons into the outgoing fibre. The automation of the output mirror's optimisation is performed as part of this thesis project, and described in Section 4.

3.3 Frequency Lock

In order to achieve a sufficient signal-to-noise ratio (SNR) for single photons at the midpoint, strict filtering is applied, consisting of two FBGs for each arm, briefly discussed Section 3.2. This strict filtering, however, means that the transmission frequencies of the two narrow FBGs (UNFs) quickly drift apart when left unchecked, diminishing any quantum effects at the midpoint beamsplitter (BS). Moreover, the frequencies of incoming ZPL photons also quickly drift outside the UNF's transmission range without active feedback. To solve these issues, an active feedback system - the frequency lock - is implemented to lock the two UNFs to the same frequency, and to lock the incoming telecom ZPL photons to the peak frequency of their respective UNF.

The frequency of the incoming telecom photons can be tuned by adjusting QFC pump laser's frequency: changing its frequency changes the telecom frequency by the same but opposite amount. Furthermore, the frequency of the UNF transmission peaks can be adjusted by changing the UNF's temperature: this expands or contracts its filter spacing, and hence changes its transmission frequency.

To generate the actual lock, the midpoint applies a single reference laser in conjunction with the phase light from the nodes. The optical setup of the filtering is shown in Figure 3.5a, showing the paths taken by the three

types of light and measurement of the error signals. To lock the UNFs to the reference light, the transmission of the reference light through the UNFs is used as error signal. Meanwhile, an interference beat between the reference and phase light is used as error signal for the telecom light. Details of the active feedback system are described in Figure 3.5b.

It should be noted that continuously running the frequency lock completely blinds the midpoint SNSPDs, rendering single photon detections impossible. Instead, bursts of phase and reference light are interleaved with actual single photon experiments. The frequency lock light is synchronised with the 5 kHz heartbeat, taking up 2.5 µs of each 200 µs time window. To sufficiently suppress the reference beam, three AOMs are used in series. However, an elevated noise level after the detector blinding makes the first 45 µs of each window unusable, leaving 155 µs per window for actual single-photon experiments.

4 QFC Output Mirror Optimisation

In this section, the results of the first project are discussed: the optimisation framework to calibrate the output mirror in the QFCs. Details of the QFCs are discussed in Section 3.2.

Working toward autonomy of the QLink Demonstrator project, the ability for elements of the system to calibrate without human intervention is crucial. One of the components for which this ability was not yet implemented in the TPQI experiments in [15], was the mirror coupling the QFC's outgoing telecom light into a fibre toward the midpoint.

4.1 Challenges

Although the QFC's output mirror is motorised and an optimisation framework exists for other motorised mirrors within the system, the existing framework cannot simply be copied to the QFC output mirror. Specifically, four other motorised mirrors are used per node: two for ZPL fibre in-coupling, and two for pump and ZPL light in-coupling into the QFC's ppLN crystal. The efficiency of these mirrors' coupling strengths can be measured by flipping in an APD at the QFC's ZPL input or a PM at the QFC's crystal output, respectively, see Figure 3.4. The light to measure the coupling is generated with green light (on the NV, generating ZPL photons) and phase light, respectively.

However, the purpose of the QFC's output mirror is to couple the QFC's outgoing telecom light into the fibre toward the midpoint, after which point there is only fibre optics until the midpoint's SNSPDs. Consequently, it is impossible to flip in an APD or PM after the fibre in-coupling, making the SNSPDs the only option to read out the coupling efficiency.

A number of challenges arise when trying to use the SNSPDs as coupling sensor. Firstly, for light to be able to reach them, a frequency lock needs to be established and kept alive. This creates the two-way dependency that the QFC's output mirror needs to be relatively well-aligned for a frequency lock to be able to be closed, while the mirror can only be calibrated with the frequency lock turned on. Secondly, as described in Section 3.3, the coupling light needs to be interleaved with phase and reference light to keep the lock alive. Thirdly, due to photon losses encountered in telecom in-coupling, transmission, midpoint filtering and photon detection, as well as noise introduced by these components, significantly more excitation light is required for a sufficient signal. Finally, the midpoint is shared by both nodes, meaning that optimisation of the QFC output mirrors of both nodes needs to be performed sequentially, or interleaved.

An additional challenge arises with the mirror's movement: a fluctuating step size difference of up to a factor 1.5 exists between taking left (up) and right (down) steps due to inherent non-deterministic physical stepsize of the used stick-slip piezo steppers, meaning that taking the same number of steps back and forth does not return the mirror to its initial position. The optimisation algorithm should take this into account: taking a large step may result in a loss of signal and hence the lock, without an option to easily return to the initial position and no way to measure the signal.

4.2 Implementation

To generate as much light as possible for testing, the objective is moved to the stripline and illuminated with up to 20 µW of readout light. This generates up to roughly a factor ten million more light in the ZPL path compared to illumating the NV centre with green light at full power. The readout light is interleaved with phase and reference light pulses at the heartbeat frequency of 5 kHz. The AWG is programmed such that, within each 200 µs window, the first 30 µs are reserved for the frequency lock pulses and noise ringoff. The remaining time within each window is then used to interleave the light from Node 1 and Node 2, at 70 µW each. The number of photons received within these time windows can then be integrated over multiple heartbeats to create an effective measure of coupling efficiency.

To effectively capture the counts generated by the SNSPDs, a monitoring tool within the QMI software framework is used. That is, the driver of the timetagger (counting the SNSPDs' photon detections), has the ability to send out live histograms, containing the counts per timebin accumulated over multiple 200 µs windows. Specifying a desired binning size and integration time, these histogram signals can then be subscribed to and used to compute the counts within the windows of Node 1 and Node 2.

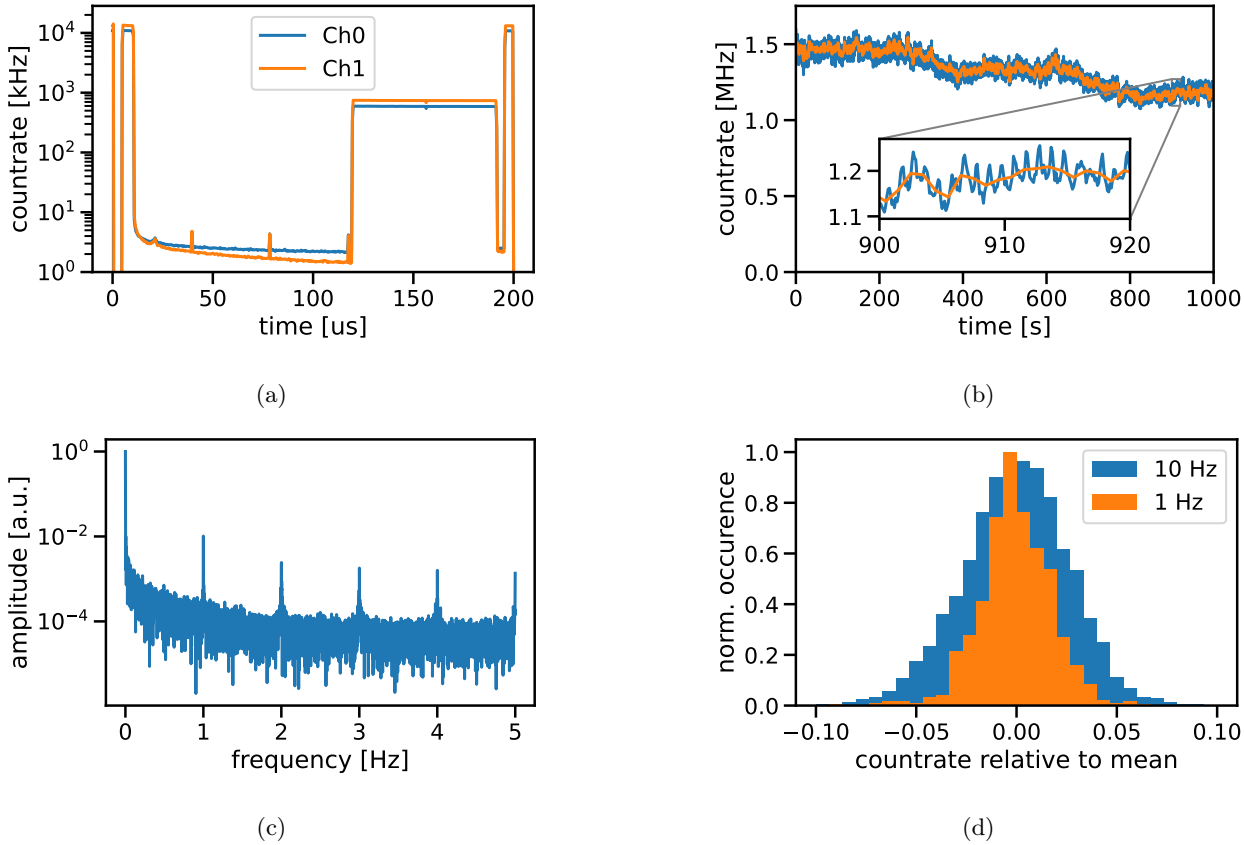

(a) (b) (c) (d)

Figure 4.1: ***(a) Countrate at the SNSPDs*** *between each heartbeat, split into 5000 bin of* 40 ns *each, and averaged for* 1000 s*. The reference light is enabled from 0-2.5 µs, the phase light is disabled from 10-195 µs, and node 2's readout light is enabled from 120-190 µs. The small peaks at 40, 80, 120 and 160 µs are artefacts from splitting up the pulse into chunks due to a known bug in the AWG driver implementation,* ***(b) Node 2 countrate*** *over time, with inset zooming in on a typical* 20 s *window. The countrate shows a slow drift, occasional jumps and a prominent* 1 Hz *oscillation,* ***(c) Countrate Fourier spectrum*** *of the 10 Hz data shown in (b). The peaks lie at precisely integer frequencies, coming from the cryostat pulse tube, oscillating at* 1 Hz *with harmonics,* ***(d) Distribution of countrate relative to its mean****, extrapolated from the data shown in (b). Low frequency drifts are filtered with a cutoff of* 60 s*.*

Within the expectation that the signal from the SNSPDs is well-behaved, a simple gradient descent algorithm is used to optimise the mirror's position. The algorithm was lightly adapted from the existing mirror optimisation framework, and is performed as follows: given an axis (e.g. the x-axis), an initial direction is chosen (e.g. left) and a step taken in said direction. If the coupling increases after this step, continue taking steps in this direction. Otherwise flip the direction (right in this case). Keep taking steps in the chosen direction for as long as the coupling improves. As soon as the coupling decreases once, stop the algorithm. Repeat for the second axis.

4.3 Results

To show the operation of the measurement and optimisation system, first the stability of the coupling signal is analysed, after which the mirrors are swept to investigate their sensitivity, and finally the optimisation algorithm is run. During the time of the measurements, only node 2 was operational, meaning that the results solely focus on this node.

An example of a histogram received from the timetagger is shown in Figure 4.1a, showing the pulse sequence to behave as intended. Importantly, an instantaneous countrate close to 1 MHz is reached per nanowire when the node 2 readout laser is enabled. This is easily sufficient for optimisation measurements. The stability of this countrate is shown in Figure 4.1b, showing a pronounced 1 Hz beat, slow drifts and occasional small jumps. The beat is attributed to vibrations of the cryostat, pumping at this frequency. Fourier analysis of the

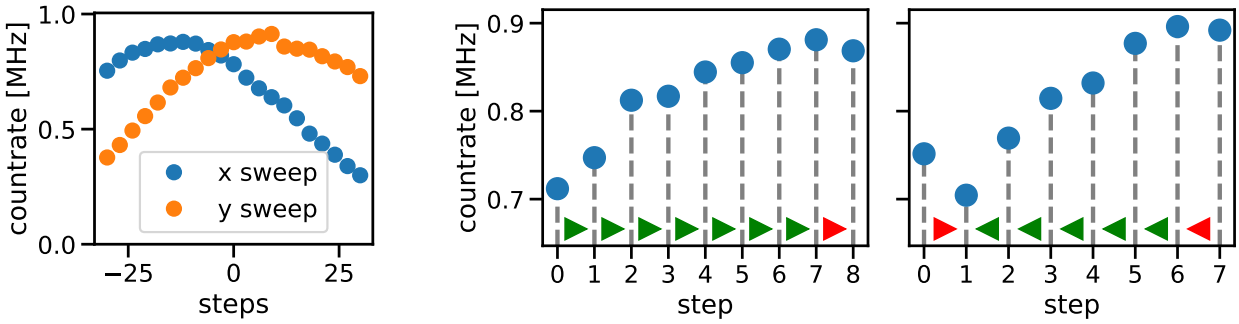

(a) (b)

Figure 4.2: ***(a) QFC output mirror sweep*** *consisting of 20 steps of size 3. Integration time per datapoints is* 1 s*, skipping every second value to avoid measuring while the mirror is still moving. The sweep started out at the optimum mirror position, and each axis was optimised between sweeps. The jump in counts during the y sweep is attributed to random fluctuations,* ***(b) QFC output mirror optimisation*** *of the x and y axis, respectively. The starting points of the optimisation are the (imperfect) returning points of the sweeps shown in (a). The arrows direction corresponds to optimisation direction, and arrow colour indicate whether the countrate has increased (green) or decreased (red). The final datapoint for both figures is the end point of the algorithm. The x optimisation starts out in the correct direction, walks to the top and one step over it, and then stops. The y optimisation starts out in the wrong direction, switches direction, and then similarly walks to the top and one step over it.*

countrate, shown in Figure 4.1c, confirms the 1 Hz beat and its harmonics as the leading noise term, showing no other contributions over the noise floor. This causes the spread of countrate data to increase significantly when integrating shorter than 1 Hz, as shown in Figure 4.1d. An integration of 1 s per datapoint is used for the remainder of this section, to avoid the 1 Hz beat but keep integration time as short as possible.

A mirror sweep is shown in Figure 4.2a, showing the countrate to halve after roughly 30 steps, and highlighting the unequal left/right step sizes. Importantly, though, the sweep shows uniformly increasing countrates almost to the top, meaning that a simple gradient ascent algorithm is indeed generally sufficient to reach close to the top with high probability. Typical results of such an optimisation are shown in Figure 4.2b. Both the gradient ascent and direction reversal are shown to operate as desired, nearly reaching the true optimal position.

4.4 Discussion and future improvements

With the use of the SNSPDs as coupling sensors working as intended, their use as such can be expanded. Firstly, the optimisation of the other two QFC mirrors can be performed using the SNSPDs. The QFC's PM has a low signal-to-noise ratio, meaning that using the SNSPDs might yield an improvement in reliability to reach the optimum position. Implementation is near-trivial, as the nanowire coupling sensor code is made to behave identically to the other coupling sensors.

Secondly, the SNSPDs, in combination with the ZPL APD, can be used to measure the efficiency of the QFC, frequency lock and telecom transmission combined. Thusfar, this efficiency has only been estimated; an actual measurement may provide insight into unknown processes, or confirm knowledge about the system. This measurement does require a trade off in readout power: the ZPL APD cannot handle a high countrate, while a factor 10 in photons is lost toward the SNSPDs, combined with a high noise floor there. Hence, a longer, low-power measurement is required to get a good signal at the midpoint while not blinding the ZPL APD.

5 Cyclicity Model

5.1 Introduction

Excited state cyclicity, meaning how well an excited state decays back to its corresponding m_s ground state after excitation, is a crucial concept for NV centre operation. High cyclicity allows for many excitation cycles and thus many emitted photons before a spin flip occurs, as well as high correlation between an emitted photon and the qubit spin state afterwards; the defining properties for good single-shot readout and spin-photon entanglement. Low cyclicity, meanwhile, allows for fast pumping to a different spin state; crucial for fast spin state initialisation at high fidelity.

The behaviour of the NV centre's excited states is well researched at low temperature, strain, and magnetic field [18]: the $m_s = 0$ excited states, $|E_{x,y}\rangle$, as well as $|A_2\rangle$ are highly cyclic and thus suitable for readout and spin-photon entanglement generation. The $m_s = \pm 1$ excited states, $|A_1\rangle$ and $|E_{1,2}\rangle$, meanwhile, have low cyclicity and are therefore ideal for spinpumping. Furthermore, the process of excited state mixing at non-zero fields and temperature is well described [19]. This chapter presents a model unifying the two, allowing for excited state cyclicity predictions over a wide range of external parameters. A particular focus will be placed on the high cyclicity of the $|E_{x,y}\rangle$ states, as their behaviour is generally limiting in NV centre operation.

In the remainder of this section, first the necessary excited state theory is explained in more detail in Section 5.2. Secondly, the implementation of the eigenstate solver used to compute the excited states is detailed in Section 5.3. Thirdly, the concept of cyclicity is presented and its impacts on readout and spin photon entanglement are discussed in Section 5.4. An overview of model predictions is presented in Section 5.5, and finally a list of known model limitations is discussed in Section 5.6.

5.2 Theory

The theory towards cyclicity is discussed in three parts: first, we describe the NV's excited state Hamiltonian, followed by its possible decay paths back to the ground state, and finally temperature mixing effects.

5.2.1 Excited state Hamiltonian

In Section 2.1.1, it was introduced that the NV centre's first excited state is split up into six distinct symmetry eigenstates, $E_{x,y}$ and $A_{1,2}/E_{1,2}$ with $m_s = 0$ and $m_s = \pm 1$, respectively. Their states are described by the eigenstates of the following Hamiltonian acting on molecular orbit and spin [4],

$$\begin{aligned}\hat{H}_{\mathrm{ES}} = & D_{\mathrm{es}}^{\parallel}\hat{S}_z^2 - \lambda_{\mathrm{es}}^{\parallel}\hat{\sigma}_y \otimes \hat{S}_z \\ & + D_{\mathrm{es}}^{\perp}\left[\hat{\sigma}_z \otimes \left(\hat{S}_y^2 - \hat{S}_x^2\right) - \hat{\sigma}_x \otimes \left(\hat{S}_y\hat{S}_x + \hat{S}_x\hat{S}_y\right)\right] \\ & + \lambda_{\mathrm{es}}^{\perp}\left[\hat{\sigma}_z \otimes \left(\hat{S}_x\hat{S}_z + \hat{S}_z\hat{S}_x\right) - \hat{\sigma}_x \otimes \left(\hat{S}_y\hat{S}_z + \hat{S}_z\hat{S}_y\right)\right],\end{aligned} \tag{5.1}$$

where $\hat{s}_i$ are the Pauli matrices acting on molecular orbit e_x, e_y, and $\hat{S}_i$ are spin-1 operators acting on the spin, $m_s = -1, 0, +1$. The constants are given in Table 5.1. The $E_{1,2}$ and $E_{x,y}$ eigenstates form degenerate energy pairs, while A_1 and A_2 have distinct energies.

Under the influence of electric and magnetic fields, the eigenenergies are known to shift due to interactions between the eigenstates, the effects of which are included by adding the following potential to the effective Hamiltonian [4],

$$\begin{aligned}\hat{V}_{\mathrm{ES}} = & d_{\mathrm{es}}^{\parallel}(E_z + \chi_z) + d_{\mathrm{es}}^{\perp}\Big((E_x + \chi_x)\hat{\sigma}_z - (E_y + \chi_y)\hat{\sigma}_x\Big) \\ & + \mu_B\left(l_{\mathrm{es}}^{\parallel}\hat{\sigma}_y + g_{\mathrm{es}}^{\parallel}\hat{S}_z\right)B_z + \mu_B g_{\mathrm{es}}^{\perp}\left(\hat{S}_x B_x + \hat{S}_y B_y\right),\end{aligned} \tag{5.2}$$

where E_i, B_i and χ_i represent the electric field, magnetic field and effective strain, respectively. The precise impact of different parameters is discussed in Section 5.5. The values of the different constants are shown in Table 5.1. In this work, the values as measured by [20] are used. Furthermore, $\mu_B = e\hbar/(2m_e h)$ Hz/T $\approx$ 13.996 GHz/T.

Parameter	Value [20]	Value (literature)
$\lambda_{\mathrm{ES}}^{\parallel}$	5.297(9)	5.3 [21]
$\lambda_{\mathrm{ES}}^{\perp}$	0.18(4)	0.14 [22]
$D_{\mathrm{ES}}^{\parallel}$	1.402(8)	1.42 [21]
$D_{\mathrm{ES}}^{\perp}$	0.80(4)	0.79 [21]
$l_{\mathrm{ES}}^{\parallel}$	0.131(5)	0.10(1) [23, 24]
$g_{\mathrm{ES}}^{\parallel}$	1.998(5)	2.01(1) [25, 26]($T = 300$K)
$g_{\mathrm{ES}}^{\perp}$	2.0	2.0

Table 5.1: *Constants used in the excited state Hamiltonian. All values are given in* GHz.

5.2.2 Excited state decay

The decay paths of the different excited states are shown in Figure 5.1(a) [19]. All excited states directly decay to the ground state with a rate of $\Gamma_1^{A_{1,2}} = \Gamma_0^{E_{x,y}} = \Gamma_1^{E_{1,2}} = 2\pi \cdot 13.2 \pm 0.5$ MHz. This decay is spin-conserving, meaning the $|E_{x,y}\rangle$ states decay to $|0\rangle$, while the $|E_{1,2}\rangle, |A_{1,2}\rangle$ states decay to $|\pm 1\rangle$.

Instead of decaying directly, the $|A_1\rangle$ excited state can additionally decay to the upper singlet state ${}^1A_1$ through spin-orbit coupling, while the $|E_{1,2}\rangle$ states can also decay to the singlet states through electron-phonon coupling with $|A_1\rangle$, as shown in Figure 5.1(c) [19]. The respective decay rates at low temperature are experimentally determined as $\Gamma_S^{A_1} = 2\pi \cdot 16.0 \pm 0.5$ MHz [19] and $\Gamma_S^{E_{1,2}} = 2\pi \cdot 8.2 \pm 0.2$ MHz [27]. The singlet rates of the $|E_{x,y}\rangle$ and $|A_2\rangle$ states, meanwhile, are predicted and determined to be negligible at low temperature and strain [19]. The lifetime of the different excited states is computed as the inverse of the total decay rate,

$$\tau_i = \frac{1}{\Gamma_G^i + \Gamma_S^i}, \tag{5.3}$$

yielding $\tau_{E_{x,y}} = \tau_{A_2} = 12.1 \pm 0.4$ ns, $\tau_{E_{1,2}} = 7.4 \pm 0.3$ ns, $\tau_{A_1} = 5.5 \pm 0.3$ ns.

Decay from the singlet states back to the ground states occurs at a significantly longer timescale of $\tau_G^S = 371 \pm 6$ ns [28], i.e. $\Gamma_G^S = 2\pi \cdot 429 \pm 6$ kHz, but its branching ratio of decay to $m_s = 0$ or $m_s = \pm 1$ has not been determined with certainty at low temperature. Theoretical models and room-temperature measurements have shown an even $2:1:1$ distribution between $m_s = 0 : +1 : -1$ [4], while the single measurement at cryogenic temperature yielded a ratio tending strongly towards $m_s = 0$, at $(8 \pm 1) : 1 : 1$, though with individual datapoints ranging between $(5 \pm 1) : 1 : 1$ and $(13 \pm 3) : 1 : 1$ [27]. For the remainder of this section, we will take the value from [27], to find $80 \pm 2\%$ branching to $|0\rangle$.

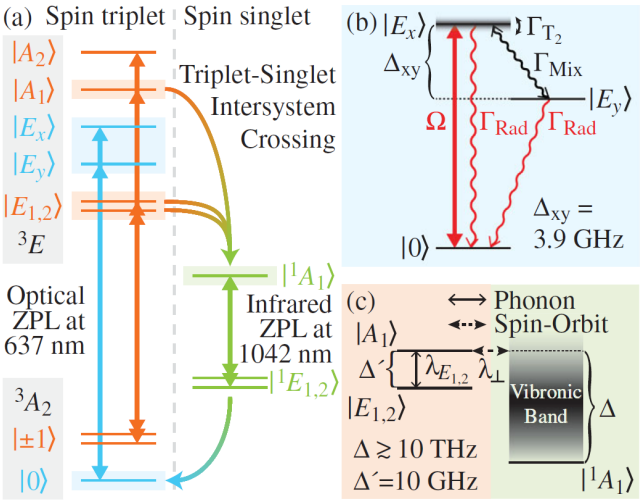

Figure 5.1: *(a) Allowed decay paths for the different excited states. All excited states decay directly to their corresponding m_s ground state. The $m_s = \pm 1$ excited states $|A_1\rangle$, $|E_{1,2}\rangle$ additionally decay to the singlet states, while the singlet states decay to the ground states, with the majority to $|0\rangle$. (b) Model for temperature mixing between the $|E_{x,y}\rangle$ states when exciting one of the two states at nonzero temperature. (c) Decay path from $|E_{1,2}\rangle$ to the singlet states via the $|A_1\rangle$ state. Figure taken from [19].*

5.2.3 Temperature mixing

The theory thus far has assumed temperatures close to absolute zero. At temperatures above $T \sim 4$K, phonon induced state mixing starts to become significant. At temperatures $T < 50$K and energy splittings $\chi \ll k_B T$, mixing between two states with the same spin m_s can occur through the two-phonon Raman process, illustrated in Figure 5.2(a). The probability of such mixing occurring between two excited states before decay scales with temperature as

$$P_{xy}(T) = P_{yx}(T) \approx \frac{1}{1 + \frac{1}{CT^5}}, \tag{5.4}$$

for energy splittings $\chi \ll k_B T$, and with $C = (9.2 \pm 0.5) \cdot 10^{-7}$ K^{-5}. All allowed mixing between excited states is illustrated in Figure 5.2(b) [18, 29].

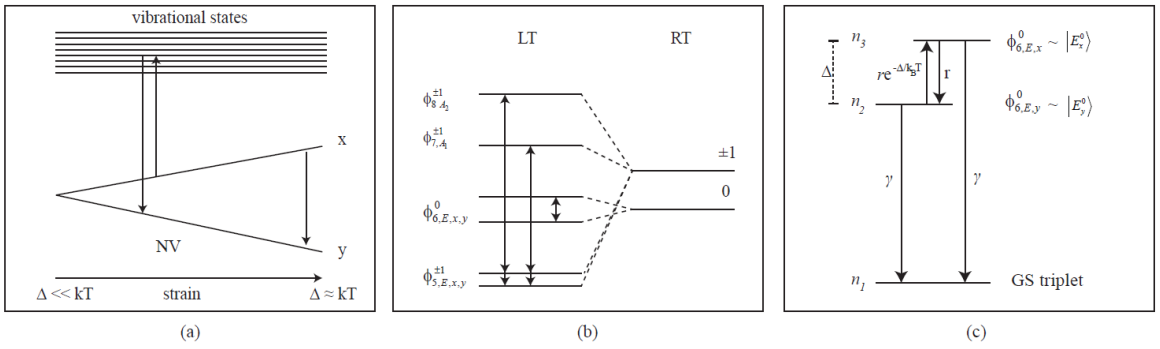

Figure 5.2: *(a) Example of the two-phonon Raman process occurring between $|E_{x,y}\rangle$ for $\chi \ll kT$, resulting in mixing between the two states. (b) Allowed transitions between the symmetry states at low temperature (LT), resulting in the net states at room temperature (RT). (c) Three-level model used to estimate the rate of mixing between two excited states. Image taken from [18]*

5.3 Computational Model

5.3.1 Numerical simulation

For each external field input, the eigenstates and eigenenergies are found numerically by solving the Hamiltonian in matrix form. That is, we write the Pauli and spin-1 operators as

$$\hat{\sigma}_x = \begin{bmatrix} 0 & 1 \\ 1 & 0 \end{bmatrix} \qquad \hat{\sigma}_y = \begin{bmatrix} 0 & -i \\ i & 0 \end{bmatrix} \qquad \hat{\sigma}_z = \begin{bmatrix} 1 & 0 \\ 0 & -1 \end{bmatrix} \tag{5.5}$$

$$\hat{S}_x = \begin{bmatrix} 0 & 1 & 0 \\ 1 & 0 & 1 \\ 0 & 1 & 0 \end{bmatrix} \qquad \hat{S}_y = \begin{bmatrix} 0 & -i & 0 \\ i & 0 & -i \\ 0 & i & 0 \end{bmatrix} \qquad \hat{S}_z = \begin{bmatrix} 1 & 0 & 0 \\ 0 & 0 & 0 \\ 0 & 0 & -1 \end{bmatrix}, \tag{5.6}$$

and $\hat{\sigma}_i \otimes \hat{S}_j$ is taken as the Kronecker product of the two matrices, forming six-by-six matrices in the molecular orbit and spin (MO) basis $E_{x,y}^{m_s}$, giving the eigenstates in the basis $\left[E_x^+, E_y^+, E_x^0, E_y^0, E_x^-, E_y^-\right]$. However, for cyclicity computations the symmetry basis, $[E_2, E_1, E_x, E_y, A_1, A_2]$, is required, as this basis defines the excited state decay characteristics. The symmetry basis functions are obtained from the MO basis functions as follows [4],

$$\phi_{E_2} = \frac{1}{\sqrt{2}}\left(\phi_{E_x^+} - i\phi_{E_y^+}\right) \qquad \phi_{E_x} = \phi_{E_x^0} \qquad \phi_{A_1} = \frac{1}{2}\left(\phi_{E_x^+} + i\phi_{E_y^+} + \phi_{E_x^-} - i\phi_{E_y^-}\right) \tag{5.7}$$

$$\phi_{E_1} = \frac{1}{\sqrt{2}}\left(\phi_{E_x^-} + i\phi_{E_y^-}\right) \qquad \phi_{E_y} = \phi_{E_y^0} \qquad \phi_{A_2} = \frac{1}{2}\left(\phi_{E_x^+} + i\phi_{E_y^+} - \phi_{E_x^-} + i\phi_{E_y^-}\right). \tag{5.8}$$

Furthermore, when applying a perpendicular strain or electric field, the angle θ of this field changes the $E_{x,y}$ eigenstates accordingly. To ease analysis, the effect is eliminated by rotating along in our picture,

$$\phi_{E_x^\theta} = \cos(\theta/2)\,\phi_{E_x} + \sin(\theta/2)\,\phi_{E_y} \tag{5.9}$$

$$\phi_{E_y^\theta} = -\sin(\theta/2)\,\phi_{E_x} + \cos(\theta/2)\,\phi_{E_y}. \tag{5.10}$$

For the remainder of this work, $E_{x,y}^\theta$ is implied when writing $E_{x,y}$. From the superpositions principle, the Hamiltonian eigenstates can be transformed in the same fashion, by rewriting the transformation to matrix form as

$$T = \begin{bmatrix} 1/\sqrt{2} & -i/\sqrt{2} & 0 & 0 & 0 & 0 \\ 0 & 0 & 0 & 0 & 1/\sqrt{2} & i/\sqrt{2} \\ 0 & 0 & \cos(\theta/2) & \sin(\theta/2) & 0 & 0 \\ 0 & 0 & -\sin(\theta/2) & \cos(\theta/2) & 0 & 0 \\ 1/2 & i/2 & 0 & 0 & 1/2 & -i/2 \\ 1/2 & i/2 & 0 & 0 & -1/2 & i/2 \end{bmatrix}. \tag{5.11}$$

It is important to discern between the zero-field symmetry functions and the Hamiltonian eigenstates. When discussing the excited states at nonzero fields, it is customary to name the eigenstates according to the symmetry state they are perturbed from. Concretely, when discussing eigenstate compositions ϕ_i implies the symmetry state, while $|i\rangle$ implies the perturbed eigenstate.

5.3.2 Tracking states over high fields

A high electric and magnetic fields, significant mixing and (avoided-)level crossings make it nontrivial to determine what eigenstate corresponds to which symmetry state. To this end, determining the sorting is performed by two distinct algorithms.

For smaller perturbations, the algorithm used by [20] is applied, which sorts the eigenstates by matching them to the symmetry states one-by-one, in order of largest eigenstate amplitude. Specifically, the row and column of the largest amplitude in the eigenvector is found, and the respective eigenstate is connected to the respective symmetry state of that row and column, after which that row and column are cleared and the step is repeated. This method is only valid when all eigenstates still have a majority overlap with their corresponding symmetry state.

For more significant mixing a proprietary algorithm is applied, which tracks the eigenenergies over the looped parameter. If two neighbouring energies cross or change from converging to diverging, their states are flipped. Although the algorithm suffices within the context of the simulations presented in this thesis, it should be noted

that the algorithm is not generally valid, and the switch between the two algorithms is currently performed at a hardcoded strain threshold. Implementation of a more elaborate or elegant algorithm is recommended in case of expanded use of the model for investigating high-field excited-state behaviour.

5.4 Cyclicity

5.4.1 Spin-flip probability

To turn the excited state decay properties into a value for cyclicity, we define the concept of spin-flip probability p_{flip}: the probability for an excited state to decay back to a ground state with a different spin value m_s [18]. This is the crucial parameter in cyclicity: a zero spin-flip probability means infinite cyclicity and vice versa. Specifically, we can define cyclicity as $1 - p_{\text{flip}}$: the probability to decay back to the same ground state after an excitation. Assuming excitation of only a single spin ground state, the value of p_{flip} determines a geometric distribution of the probability to remain in the original spin state for exactly k excitations: $P_{\text{cycle}}(k) = (1-p_{\text{flip}})^{k-1} p_{\text{flip}}$. This additionally determines the mean number of excitations before a spin flip, which in case of a geometric distribution equals $\langle n_{\text{cycle}} \rangle = 1/p_{\text{flip}}$.

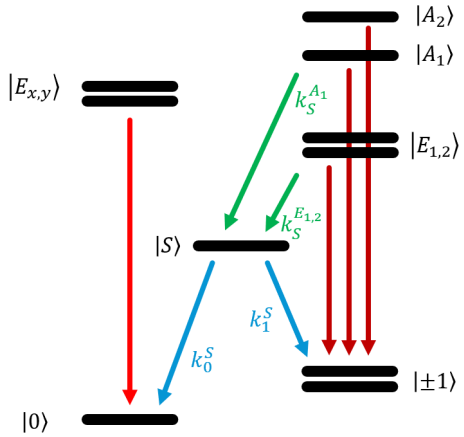

Figure 5.3: *Decay paths of the first excited states, with the possible decay paths shown. All excited states show direct decay to their corresponding ground state. The $|A_1\rangle$ and $|E_{1,2}\rangle$ states additionally decay to the singlet states with branching ratio k_S^i. The singlet states decay to the ground states with branching $k_{0,1}^S$.*

Singlet decay, field-induced state mixing and temperature-induced state mixing together define the spin-flip behaviour of an excited state. First, let us rewrite the singlet decay in terms of branching ratios into and out of the singlet states,

$$k_S^{A_1} = \frac{\Gamma_S^{A_1}}{\Gamma_S^{A_1} + \Gamma_1^{A_1}} \approx 0.55 \tag{5.12}$$

$$k_S^{E_{1,2}} = \frac{\Gamma_S^{E_{1,2}}}{\Gamma_S^{E_{1,2}} + \Gamma_1^{E_{1,2}}} \approx 0.38 \tag{5.13}$$

$$k_0^S \approx 0.8 \tag{5.14}$$

$$k_1^S \approx 0.2, \tag{5.15}$$

as defined in Figure 5.3. We then find the following spin flip probabilities for all excited states,

$$p_{\text{flip}}\left(|A_1\rangle\right) = k_S^{A_1} k_0^S \approx 0.44 \tag{5.16}$$

$$p_{\text{flip}}\left(|E_{1,2}\rangle\right) = k_S^{E_{1,2}} k_0^S \approx 0.31 \tag{5.17}$$

$$p_{\text{flip}}\left(|A_2\rangle\right) = 0 \tag{5.18}$$

$$p_{\text{flip}}\left(|E_{x,y}\rangle\right) = 0 \tag{5.19}$$

However, we are ultimately interested in the spin flip probabilities for perturbed eigenstates. Writing the composition of a state in the symmetry basis $|\psi\rangle \equiv \vec{c} = \left[c_{E_2}, c_{E_1}, c_{E_x}, c_{E_y}, c_{A_1}, c_{A_2}\right]^T \equiv \left[c_1, c_2, c_3, c_4, c_5, c_6\right]^T$,

the spin flip probabilities for $m_s = 0$ and $m_s = \pm 1$ can be written as

$$\begin{aligned} p^0_{\text{flip}}(|\psi\rangle) &= \left(|c_1|^2 + |c_2|^2\right)\left(1 - k_S^{E_{1,2}} k_0^S\right) \\ &\quad + |c_5|^2 (1 - k_S^{A_1} k_0^S) \\ &\quad + |c_6|^2, \end{aligned} \tag{5.20}$$

$$\begin{aligned} p^{\pm 1}_{\text{flip}}(|\psi\rangle) &= \left(|c_1|^2 + |c_2|^2\right) k_S^{E_{1,2}} k_0^S \\ &\quad + \left(|c_3|^2 + |c_4|^2\right) \\ &\quad + |c_5|^2 k_S^{A_1} k_0^S \\ &= 1 - p^0_{\text{flip}}(|\psi\rangle). \end{aligned} \tag{5.21}$$

The effects of nonzero temperature can now be included into the spin flip value as a linear combination of the different terms, according to the mixing rates discussed in the previous section,

$$p_{\text{flip}}(|E_{1/2}\rangle) = (1 - 2P_{xy}) p^{\pm 1}_{\text{flip}}(|E_{1/2}\rangle) + P_{xy} p^{\pm 1}_{\text{flip}}(|A_1\rangle) + P_{xy} p^{\pm 1}_{\text{flip}}(|A_2\rangle) \tag{5.22}$$

$$p_{\text{flip}}(|E_{x/y}\rangle) = (1 - P_{xy}) p^0_{\text{flip}}(|E_{x/y}\rangle) + P_{xy} p^0_{\text{flip}}(|E_{y/x}\rangle) \tag{5.23}$$

$$p_{\text{flip}}(|A_{1/2}\rangle) = (1 - 2P_{xy}) p^{\pm 1}_{\text{flip}}(|A_{1/2}\rangle) + P_{xy} p^{\pm 1}_{\text{flip}}(|E_1\rangle) + P_{xy} p^{\pm 1}_{\text{flip}}(|E_2\rangle). \tag{5.24}$$

It should be noted that these mixing rates are only valid at low electric or magnetic field strengths: due to mixing between states with different m_s values, the mixing rules presented in Figure 5.2(b) strictly do not apply anymore. However, the setup discussed in this thesis should operate at liquid helium temperature $T = 4.2$K, where temperature effects are close to negligible. Hence, a more detailed temperature model was deemed outside the scope of this work. In case the model will be used for higher temperatures, the overlap in m_s value between excited states should be used to determine mixing instead.

5.4.2 Photon emission

The number of photons emitted by a transition during continuous driving is strongly linked to cyclicity. For an ideal transition with unit probability to emit a photon during decay, the mean number of emitted photons is equal to the mean number of cycles before a spin flip $\langle n_{\text{cycle}} \rangle$, which in turn is precisely equal to the inverse of the spin flip probability,

$$\langle n_{\text{cycle}} \rangle = \frac{1}{p_{\text{flip}}}. \tag{5.25}$$

For a complete picture of non-ideal state, both the probability of non-radiative decay back to the correct ground state and radiative decay to the wrong ground state are taken into account,

$$\langle n_{\text{photon}} \rangle = p_{\text{photon | no flip}} \langle n_{\text{cycle}} \rangle + p_{\text{photon | flip}}. \tag{5.26}$$

Similarly to the spin-flip probability derivation above, the probability for a visible photon to be emitted given a decay event equals the fractional term of direct decay or singlet decay, respectively. That is, at zero temperature,

$$p^0_{\text{photon | no flip}}(|\psi\rangle) = \frac{\left(|c_3|^2 + |c_4|^2\right)}{1 - p^0_{flip}} \tag{5.27}$$

$$p^0_{\text{photon | flip}}(|\psi\rangle) = \frac{\left(|c_1|^2 + |c_2|^2\right)\left(1 - k_S^{E_{1,2}}\right) + |c_5|^2 (1 - k_S^{A_1}) + |c_6|^2}{p^0_{flip}} \tag{5.28}$$

$$p^{\pm 1}_{\text{photon | no flip}}(|\psi\rangle) = \frac{\left(|c_1|^2 + |c_2|^2\right)\left(1 - k_S^{E_{1,2}}\right) + |c_5|^2 (1 - k_S^{A_1}) + |c_6|^2}{1 - p^{\pm 1}_{flip}} = p^0_{\text{photon | flip}} \tag{5.29}$$

$$p^{\pm 1}_{\text{photon | flip}}(|\psi\rangle) = \frac{\left(|c_3|^2 + |c_4|^2\right)}{p^{\pm 1}_{flip}} = p^0_{\text{photon | no flip}}. \tag{5.30}$$

For nonzero temperatures, the same extension as presented in the previous section can be applied.

5.4.3 Single-shot readout fidelity

Readout fidelity is defined by the probability to detect at least one photon when in the 'bright state' $|0\rangle$, written as F_0, and no photons when in the 'dark state' $|\pm1\rangle$, written as $F_{\pm1}$. The total readout fidelity is the mean of the two partial fidelities, $F = \frac{1}{2}(F_0 + F_{\pm1})$. The cyclicity model does not take into account any effect which could generate unwanted light in the dark state, so no light in dark state is assumed, $F_{\pm1} = 1$. Then, the maximum fidelity is limited by probability not to detect any photons when in the bright state: $F_0 = 1 - p_{\text{no photon}}$. The photon distribution follows a geometric distribution. Such a distribution with mean λ has zero-probability $p(0) = e^{-\lambda}$, so we find the ideal fidelity readout as

$$F = 1 - \frac{1}{2}e^{-\langle n^{\text{det}}_{\text{photon}}\rangle}, \tag{5.31}$$

with $\langle n^{\text{det}}_{\text{photon}}\rangle$ the mean number of detected photons during a single excitation. This value is related to the number of emitted photons by the photon detection efficiency, η_{det}, as $\langle n^{\text{det}}_{\text{photon}}\rangle = \eta_{\text{det}}\langle n_{\text{photon}}\rangle$.

5.4.4 Spin-photon correlation

Spin-photon correlation is also defined by spin-flip probability, but now selected on receiving a photon. Ideally for spin-photon entanglement, if photon a photon is emitted, then the qubit is found in the bright ground state. Note that the current model does not take into account accidental excitation when in the dark ground state, so only the driven state is taken into account. An error can only error when a photon is emitted, but a spin flip also occurs. That is,

$$\text{SPcorr}^{0,\pm1}(|\psi\rangle) = 1 - p^{0,\pm1}_{\text{photon | flip}}(|\psi\rangle). \tag{5.32}$$

Whats more, if strict frequency filtering is applied (more strict than the ground state splitting), then erroneous photons are always filtered out. In that case, the model predicts perfect spin-photon correlation, with the only downside being a decrease in photon rate. However, it should be noted that a drop in fidelity can still be encountered if multiple attempts at spin-photon entanglement are performed sequentially without reinitialisation, allowing a spin flip to occur during one of the later pulses.

5.5 Simulation predictions

The implementation of the model can simulate over any of the three degrees of freedom of the three fields $\vec{\chi}, \vec{E}, \vec{B}$ with effect on the potential introduced in Equation 5.2, as well as temperature T. Due to the NV centre's symmetry axis in the z direction, the model is simulated in cylindrical coordinates for improved insight, meaning we get the following degrees of freedom, $[F_z, F_\perp, \theta_{F_\perp}]$ for the fields $\hat{F} = \chi, E, B$. The strain and electric field have the same impact, but can be set and/or swept separately. The terms will be used interchangeably in the remainder of this work.

As shown in Figure 2.1(c,d) introducing the NV centre's energy levels over external fields, perpendicular strain/electric field $E_\perp$ and parallel magnetic field B_z are most relevant to an NV centre's behaviour. Strain is naturally occurring and can be adjusted using DC Stark tuning. While the parallel electric field component only shifts all transition energies together, the perpendicular field has a significant impact on the excited state behaviour. Furthermore, the angle of the strain has an impact on the specific state mixing due to the finite rotational symmetry of the NV centre.

Meanwhile, while not naturally present, a nonzero parallel magnetic field B_z is generally applied to the NV centre by design. This, in the first place, is to lift the degeneracy of the $m_s = \pm1$ ground states for qubit operation, though it requires only a small field of tens of Gauss. Secondly, it is done to achieve control over C^{13}-spins in the environment, for which higher fields in the range of $B_z = 1000 - 2000$ Gauss are used to achieve higher coherence times [20]. Understanding the impact on cyclicity of these high magnetic fields is therefore also relevant. Perpendicular magnetic field is undesirable as it induces spin mixing in the NV ground state of the eigenstates, thus fields in that direction are specifically tuned to zero for experimental purposes and therefore not considered in this work [20].

5.5.1 Perpendicular electric field

The simulated eigenstate energies as a function of perpendicular electric field or strain are shown in Figure 5.4a. These energies have been studied for decades [24], and will therefore not be discussed in detail here. For readout, it is relevant to note that the $|E_y\rangle$ state crosses the $|E_{2,1}\rangle$ states at around $\chi_\perp \approx 7.5$ GHz and

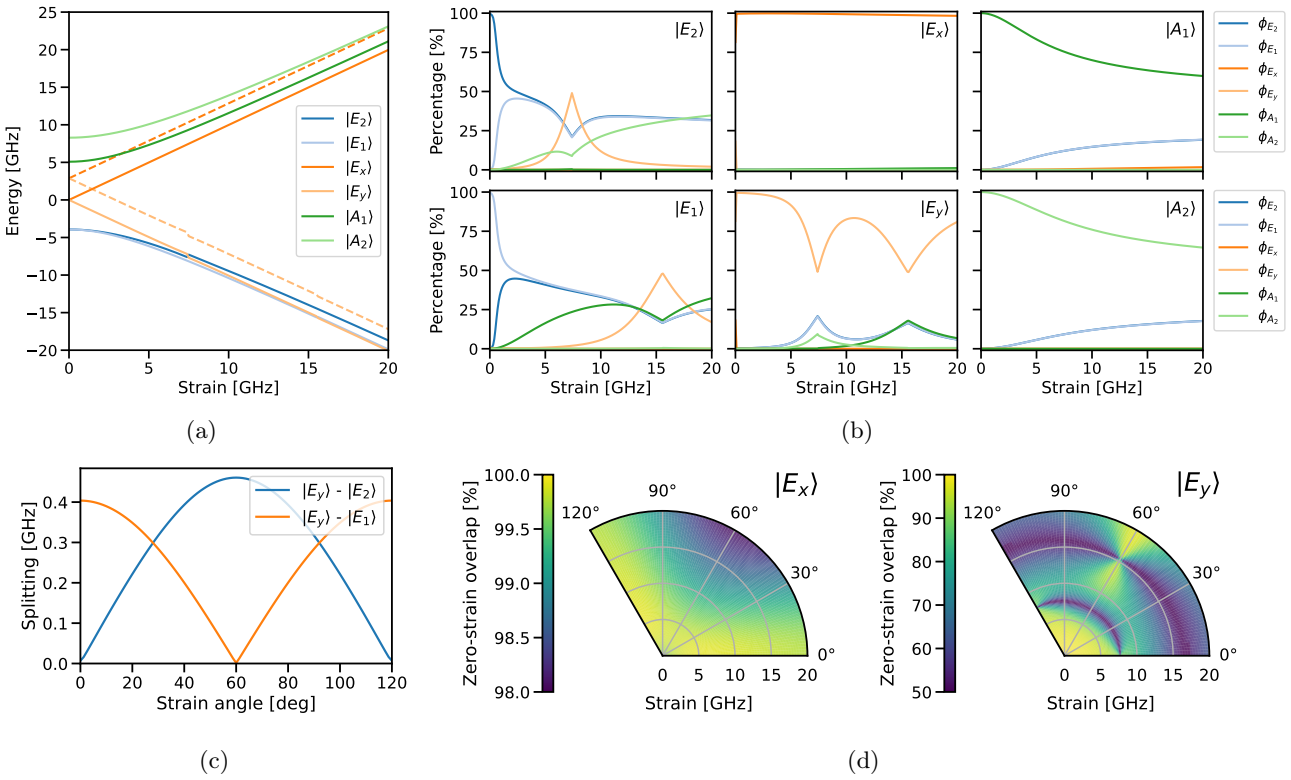

Figure 5.4: *Impact of perpendicular strain on excited states. (a) energies over strain, showing energies splitting with increased strain. The dashed orange lines show the apparent locations of the $m_s = 0$ excited states relative to the $m_s = \pm 1$ states as measured, which includes the NV ground state splitting. The $|E_y\rangle$ line crosses the $|E_{2,1}\rangle$ lines at roughly 7.5 GHz and 16 GHz, respectively. (b) Eigenstate compositions over strain viewed in the symmetry basis, at the strain angle $\theta = 45°$. The dips in $|E_y\rangle$ purity and $|E_{1,2}\rangle$ purity correspond to the energy crossings of the respective states. (c) Minimum energy splitting between $|E_y\rangle$ and $|E_{1,2}\rangle$ as a function of strain angle. Curves follow a sinusoidal shape with half period 120°, offset by 60°. (d) Overlap of the $|E_{x,y}\rangle$ eigenstates with their corresponding symmetry functions $\phi_{E_{x,y}}$ over strain and angle. Two bands of decreased overlap are observed for $|E_y\rangle$ at its energy crossings, while $|E_x\rangle$ overlap always remains above 98%.*

$\chi_\perp \approx 16$ GHz, respectively, whereas the $|E_x\rangle$ does not cross any other lines. Indeed, as shown in Figure 5.4a, $|E_x\rangle$ stays nearly completely pure over strain, whereas $|E_y\rangle$ fully mixes with $|E_{2,1}\rangle$ at the crossings. This mixing has a detrimental effect on $|E_y\rangle$ cyclicity, as will be shown further on in this section. Significant mixing also occurs between all the $m_s = \pm 1$ states, and especially between $|E_{1,2}\rangle$, which become almost fully mixed at strain levels over a couple GHz. Although outside the scope of this thesis, it predicts that $|E_{1,2}\rangle$ should lose their distinct $m_s = +1, -1$ coupling at higher strain levels.

The angle the perpendicular strain makes relative to the diamond lattice does not have a direct impact on the NV centre's excited state energy levels. Instead, it changes the interaction strengths between the different eigenstates. In particular, as shown in Figure 5.4c, the strain angle fully defines the interactions between $|E_y\rangle$ and $|E_{1,2}\rangle$, behaving as two precisely out-of-phase absolute sinoids with a half-period of 120°. For common strain regimes around a couple GHz, it means that the strain angle has a large impact on the purity of the $|E_y\rangle$ eigenstate, and hence its usability. A detailed view of $|E_{x,y}\rangle$ purity, that is, the overlap between eigenstate and its corresponding zero-field symmetry state $\phi_{E_{x,y}}$, is plotted in Figure 5.4d as a function of strain and angle. In the right plot, showing the purity of $|E_y\rangle$, the crossings with $|E_{1,2}\rangle$ are clearly visible as bands of 50% purity. For any angle except precisely 0° and 60° (mod 120°), the purity drops to 50%; only the width in strain of the drop changes. The left plot, showing $|E_x\rangle$ purity, shows that this eigenstate remains relatively pure over strain and angle, with a purity ranging between $98.0 - 99.8\%$ at $\chi = 20$ GHz, depending on strain angle. This angular dependency is attributed to $|E_x\rangle - |A_1\rangle$ interaction, with a suspected similar angular dependence in interaction strength as $|E_y\rangle - |E_{1,2}\rangle$.

5.5.2 Parallel magnetic field

The eigenstate energies over strain, but now with an added parallel magnetic field B_z are shown in Figure 5.5b. The $|E_{x,y}\rangle$ energies do not change, while the $|E_{1,2}\rangle$ and $|A_{1,2}\rangle$ pairs move apart in energy. In Figure 5.5c it can be observed that the magnetic field changes which energy levels cross, and what strain level: at $B_z \approx 200$ G, the $|E_y\rangle - |E_1\rangle$ crossing disappears; at $B_z \approx 700$ G, $|A_1\rangle$ starts crossing $|E_x\rangle$; at $B_z \approx 1300$ G, $|E_2\rangle$ has moved up in energy such that it now crosses $|E_x\rangle$ instead of $|E_y\rangle$; and finally, at $B_z \approx 1900$ G, $|E_2\rangle$ and $|A_1\rangle$ cross. At even higher magnetic fields, $|A_1\rangle$ will switch to crossing $|E_y\rangle$, but that is outside the general magnetic field regime applied to NV centres.

In Figure 5.5b, the eigenstate compositions at and up to $B_z = 1000$ G are shown. Most notable are the shifting strain levels at which the eigenstates cross, especially the new crossing between $|E_x\rangle$ and $|A_1\rangle$. Whereas without magnetic field the $|E_x\rangle$ state remains almost completely pure over strain while $|E_y\rangle$ mixes, it is now strain and magnetic field dependent which state is more pure. This should be taken into account when increasing or changing magnetic field regime. Furthermore, compared to zero magnetic field, the $|E_{1,2}\rangle$ states become more pure, while the $|A_{1,2}\rangle$ states become more mixed. It is claimed that at higher magnetic fields, the molecular orbit basis more accurately reflects the eigenstates [20], although deeper analysis is outside the scope of this work.

Finally, analysis of the splitting $|E_y\rangle - |E_2\rangle$ and $|E_x\rangle - |A_1\rangle$ over angle and magnetic field strength, shown in Figure 5.5d, reveals that the angular dependence of the interaction changes with magnetic field: the former converges to a consistently present interaction term before for higher magnetic field, while the latter maintains its dependence and even changes sign direction at towards $B_z = 2000$ G. The $|E_y\rangle - |E_1\rangle$ interaction shows the same behaviour as $|E_y\rangle - |E_2\rangle$, while the $|E_x\rangle - |E_2\rangle$ interaction does not show an angular dependence. Hence, it is strongly dependent on exact conditions whether strain angle is important, though a full analysis is deemed outside the scope of this work.

5.5.3 Cyclicity

Using the eigenstate compositions computed in the previous two sections, the resulting spin-flip probability of all eigenstates over strain and magnetic field are computed and shown in Figure 5.6a. As expected, it shows high cyclicity for the $m_s = 0$ states $|E_{x,y}\rangle$ everywhere except around energy crossings, and low cyclicity for the $m_s = \pm 1$ states everywhere except for $|A_2\rangle$ at zero strain and magnetic field. This reconfirms the common use of the states for state readout and spinpumping, respectively. The divergent cyclic behaviour and possible uses of the $|A_2\rangle$ state at low fields are not discussed further in this work.

To show the strain angular dependence of cyclicity at low magnetic fields, the range of cyclicity values over strain angle are shown in Figure 5.6b for zero magnetic field and strain up to $\chi = 10$ GHz, split by m_s. It should be noted that strain regimes higher than this value are rarely encountered or applied, and are therefore excluded for the remainder of this discussion. Firstly focusing on the $m_s = 0$ readout states, the cyclicity of $|E_x\rangle$ always remains above 99.5%, and depending on strain angle continues hovering around 99.9% cyclicity up to $\chi = 10$ GHz, meaning near-ideal behaviour. The cyclicity of $|E_y\rangle$ on the other hand, while starting at the same cyclicity for zero strain, deteriorates to below 90% cyclicity at a strain of > 7.5GHz for even its most ideal angle; a twenty to hundred fold decrease in cyclicity compared to $|E_x\rangle$. Moreover, for non-ideal strain angles, the cyclicity drops down to as low as 60% around the $|E_2\rangle$ crossing at 7.5 GHz. Irrespective of strain angle, the dip drops to the same value due to perfect mixing at the crossing; only the width of the dip changes with strain angle. Furthermore, the $|E_y\rangle - |E_2\rangle$ crossing is similarly visible in the cyclicity of the $m_s = \pm 1$ states, where the $|E_2\rangle$ shows a comparable strain angle dependent dip in cyclicity as $|E_y\rangle$. Generally, the $|E_{1,2}\rangle$ and $|A_1\rangle$ transitions all three maintain low cyclicity irrespective of strain angle, making the strain angle irrelevant for normal operation. Finally, the highly cyclic behaviour of the $|A_2\rangle$ transition at low strain is maintained irrespective of strain angle.

We continue the cyclicity discussion with resulting mean photon counts $\langle n_{\text{photon}} \rangle$ for only the readout transitions $|E_{x,y}\rangle$, as the other transitions are not generally used as such. The resulting $\langle n_{\text{photon}} \rangle$ values at zero magnetic field are shown in Figure 5.6c, for strain up to $\chi = 10$ GHz and a halfway strain angle of 20°. Additionally, the effect of sample temperature on mean photon count is included, for temperatures up to $T = 20$ K. Although not shown, the photon probability per cycle always remains close to unity, except near the $|E_y\rangle - |E_2\rangle$ crossing, yet even there it stays around 80%. Consequently, viewing the mean photon number as the inverse of the spin-flip probability is a valid approximation in most practical situations, though the figures all show data from the full computation. Note that all values presented in this section are the number of emitted photons,

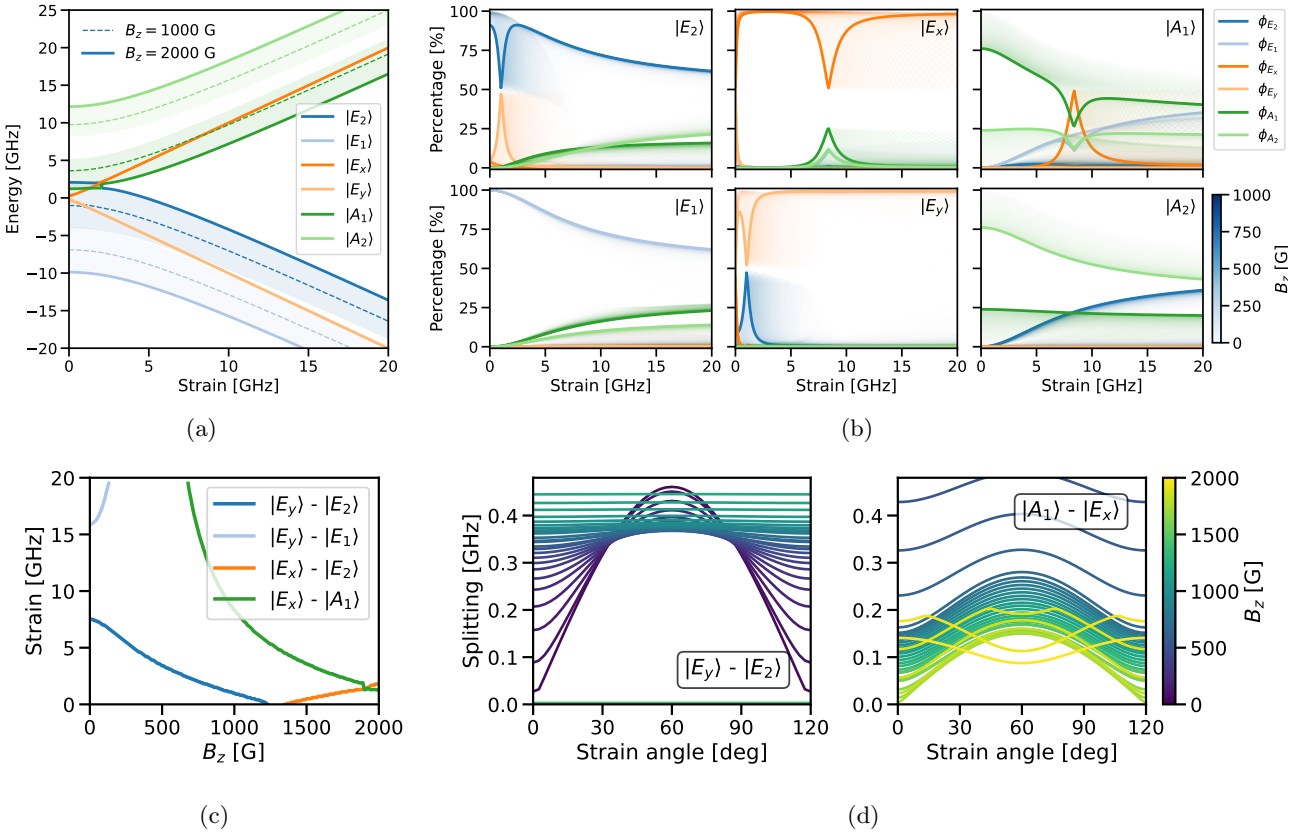

Figure 5.5: *Impact of parallel magnetic field on excited states (a) Excited state energies as a function of strain, for a magnetic field strength of* $B_z = 2000$ G *(solid) and* $B_z = 1000$ G *(dotted). The shaded area indicates the energy shifts compared to zero magnetic field strength. (b) Eigenstate compositions over strain for a magnetic field strength of* $B_z = 1000$ G *(solid lines), and the shift compared to zero magnetic field (shaded area). Compared to zero magnetic field, the* $|E_y\rangle - |E_2\rangle$ *crossing has moved to lower strain, the* $|E_y\rangle - |E_q\rangle$ *crossing has disappeared and a new* $|E_x\rangle - |A_1\rangle$ *crossing has appeared. The* $|E_{1,2}\rangle$ *states remain more pure over strain, while the* $|A_{1,2}\rangle$ *statesmix more significantly. (c) Strain levels at which specific energy crossings occur, given a magnetic field strength. Above* $B_z \sim 150$ G *and below* $B_z \sim 700$ G*, no energy crossings exist between* $|E_x\rangle$ / $|A_1\rangle$ *and* $|E_x\rangle$ / $|A_1\rangle$*, respectively. (d) Energy splittings* $|E_y\rangle - |E_2\rangle$ *and* $|E_x\rangle - |A_1\rangle$ *as a function of strain angle, for increasing magnetic field strength. A decrease in angular dependence with magnetic field is observed for the former, while an increase and reversal in angular dependence is observed for the latter.*

not the number of detected photons. Photon detection efficiency is highly setup dependent, and is assumed around 5% for this discussion. For sufficient readout fidelity, a mean photon detection count in the order of $\langle n_{\text{photon}}^{\text{det}} \rangle \sim 10$ is generally desirable, meaning a minimum emission of $n_{\text{photon}} > 100$.

At zero strain and zero temperature, the mean photon count starts at the same value of $\langle n_{\text{photon}} \rangle \approx 350$ for both $|E_x\rangle$ and $|E_y\rangle$, but diverges towards several GHz strain. For all temperatures, $|E_y\rangle$ counts quickly drop to an unusably low level around 3-4 GHz of strain. Conversely, $|E_x\rangle$ counts actually rise with increased strain at low temperature, and maintain a usable level over the entire strain range. Only with temperature do $|E_x\rangle$ counts drop as mixing increases, with higher strain levels becoming less usable with temperature. Low strain levels, however, counts always remain usable.

At higher magnetic field, the situation changes significantly. While $|E_y\rangle$ behaviour is limited by crossings at low magnetic field, the crossings shift away when increasing the magnetic field strength, as was shown in Figure 5.5c. At higher magnetic fields, it is actually the $|E_x\rangle$ transition whose behaviour is limited by crossings, particularly around $B_z \sim 1500 - 2000$ G; the magnetic regime commonly used for C^{13}-spin control. As seen in Figure 5.6d, at the common strain levels around a few GHz, the $|E_x\rangle$ transition becomes unusable. It is then precisely the $|E_y\rangle$ transition which becomes more usable, though an undesirable regime exists around $B_z \sim 1500$ G and low strain where both transitions are unusable. Opposite to low magnetic field, higher strain regimes provide higher cyclicity at high magnetic field.

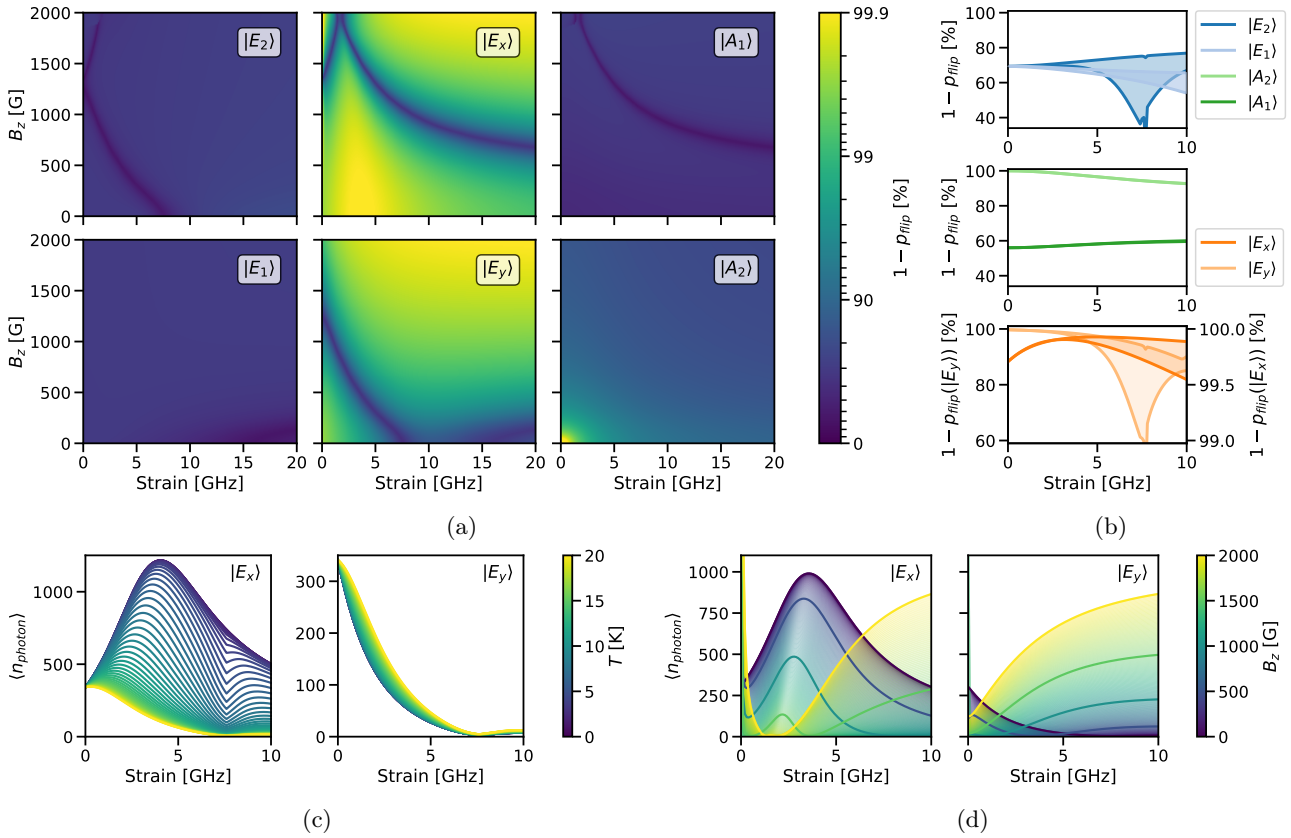

Figure 5.6: *Excited state cyclicity predictions over perpendicular strain and parallel magnetic field. (a) Predicted cyclicity for all eigenstates as a function of perpendicular strain and parallel magnetic field, for a set angle* $\theta = 30°$*. The increases in spin-flip probability correspond to energy crossings. (b) Range of possible cyclicities over strain angle, for the* $m_s = \pm 1$ *states and* $m_s = 0$ *states, respectively, at zero magnetic field. The decrease in* $|E_y\rangle$ *and* $|E_2\rangle$ *cyclicity corresponds to their energy crossing. (c) Predicted mean number of photons for* $|E_{x,y}\rangle$ *over strain and temperature, at* $\theta = 20°$ *and* $B_z = 0$ *G. At zero strain, the photon count is precisely equal for both states. (d) Predicted mean number of photons for* $|E_{x,y}\rangle$ *over strain and magnetic field, at* $\theta = 30°$ *and* $T = 0$ K.

The model and code allow for rapid investigation into these topics, which is advised for future setups applying high magnetic fields.

5.6 Known limitations

As this model focuses on the impact of external parameters on excited state cyclicity, a number of physical effects related to driving the transitions were not included in the model for clarity and time. Additionally, a number of further uncertainties and omissions are known to the author. The full list of known limitations is shown below:

- Ground state energy splitting $|0\rangle - |\pm 1\rangle$: beyond energy crossings in the excited state, the difference in energy between the ground states can additionally create crossings in transition energies, such as around $\chi_\perp = 3.5$ GHz for low magnetic field, when the $|0\rangle \rightarrow |E_x\rangle$ and $|\pm 1\rangle \rightarrow |A_1\rangle$ energies cross. This makes selective driving of the transitions impossible there.

- Homogeneous and power broadening: closely linked to the previous point, the lines of the transitions are not infinitesimally small. This means that off resonant laser light may still excite a transition.

- Distinction between $m_s = +1$ and $m_s = -1$: at zero strain or high magnetic field, the $|E_{1,2}\rangle$ excited states are selective to precise spin, both in excitation and decay [19]. For more advanced simulations, this may be important to take into account.

- Light polarisation: the different excited states have different polarisations, ranging from linear to circular. Moreover, excited state mixing will change the effective polarisations. This needs to be taken into account when driving a transition.
- Approximate temperature mixing computation: as mentioned in the main text, the temperature mixing computation is only accurate at low mixing rates; higher mixing rates would require a more elaborate algorithm taking the inner product between state vectors. Furthermore, the mixing equation is only valid over a limited temperature and energy difference range. A more advanced model is required for continued predictions at temperatures well above $T = 4$ K.
- Uncertainty in $k^S_{0/1}$: the best known literature value for the singlet branching ratio at low temperature has a large error bar, while it has a large impact on cyclicity calculations. For more accurate predictions, this value should be measured more accurately. Moreover, it is unknown whether the branching ratio has a strain or magnetic field dependence.
- Unknown stability of singlet branching over external fields: similar to the last point, the excited state decay rate into the singlet states is dependent on overlap in eigenfunctions between the triplet and singlet states, which may cause a dependence on strain and magnetic field. This possible dependence should be measured for a more accurate insight.
- No uncertainty calculation in model output: no attempt has been made to transform the uncertainties in the model's input parameters to the model's outputs. Due to the eigenstate solver step between the input and output values, a direct computation is not feasible. Hence, a Monte Carlo simulation is proposed. The implementation of such a simulation is outside the scope of this work, but advised for continued use of the model.

6 Experimental Methods

This chapter details the measurements performed for the validation of the cyclicity model described in Chapter 5. The chapter is split up into two parts: first, common NV centre operations are described, which are required for the second part describing the specific measurements to verify the cyclicity model, which will be executed in Chapter 7.

6.1 Common NV operations

The section lists a number of common operations to control NV centres, and which are required for model verification measurements. The measurements are not discussed in detail; they are mostly explained for acknowledgement, clarification and referencing.

6.1.1 Strain tuning

It is often desirable to change the NV centre's strain for experiments, particularly perpendicular strain in the case of this work. This is generally achieved through DC Stark tuning by applying a constant voltage across the NV centre, which induces a perpendicular electric field across the NV and thus provides effective strain. A crucial downside of this form of strain tuning, is that no green repumping can be used when a voltage is present, as it permanently shift charges in the environment [30]. Instead, resonant yellow repumping is required, which requires active feedback to keep the yellow laser light on resonance with the ionisation transition.

6.1.2 Linescan

A common way to find the precise excited state transitions is to perform a sweep over a wide range of frequencies, and to see at which frequencies the NV centre responds with light emission. Figure 6.1 shows the diagram of such a linescan for yellow repumping. It is important to note that the yellow laser may drift off resonance during the sweep, in which case the signal is lost after an ionisation event.

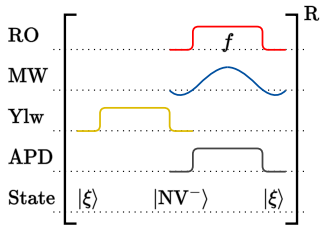

Figure 6.1: *Diagram showing the operations for a linescan. At every frequency step, the NV is deionised with a yellow laser pulse, after which the readout laser is fired while checking the PSB APD for counts. This shows a high level of counts when on resonance with one of the* $m_s = 0$ *eigenstates. Continuous microwave driving can be added alongside to also reveal* $m_s = \pm 1$ *transitions. This process is repeated a number of times for each frequency step to get sufficient photon statistics.*

6.1.3 Charge-resonance check

Before starting any experiment, it is important to make sure that that the NV centre is in the correct charge state and that the lasers are on resonance with their respective transitions. These two operations are performed together in a Charge-Resonance (CR) check. A diagram showing the operations for both green and yellow repumping is shown in Figure 6.2.

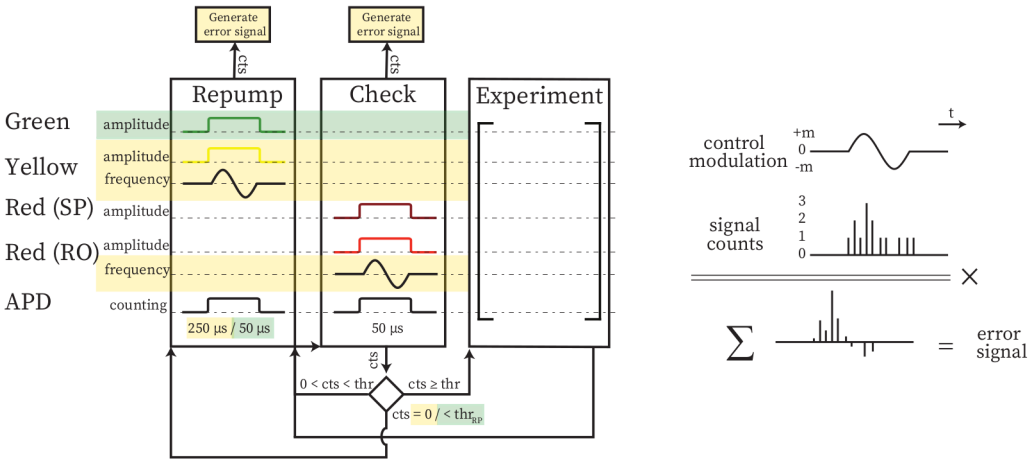

Figure 6.2: *Diagram showing the process of CR checking, which is performed before starting a measurement. Image taken from [8]. During a charge-resonance check, first the repumping laser is fired, which should bring the NV to the negative charge state if it was ionised. Afterwards, the spinpump and readout laser are fired simultaneously. If both lasers are on resonance, this should continuously excite the NV, emitting many photons in the process. The photons detected in the PSB during this resonance check determine the next step, according to two thresholds. If the photon count exceeds the 'hard' threshold, the NV is deemed on resonance and the actual measurement is started. If the counts fall in between the 'soft' and 'hard' threshold, the NV is deemed off-resonant but not ionised, and the resonance check is repeated. If the counts are below the 'soft' threshold, the NV is deemed ionised and repumping is initiated. To keep the lasers on resonance, the readout laser frequency –and yellow laser frequency in case of yellow repumping– are swept up and down during their driving. The counts as a function of laser frequency as then used to generate an error signal and fed back to the laser frequencies. The spinpump transition generally does not require this feedback mechanism due to the wider $m_s = \pm 1$ transitions and higher laser powers.*

6.1.4 Single-shot readout

One of the most important operations on an NV centre is to determine its electronic spin state. The cyclicity of the $m_s = 0$ transitions allows for single-shot readout of the spin state, meaning a high probability to discern between $|0\rangle$ and $|\pm 1\rangle$ for single state by driving one of the $m_s = 0$ transitions and checking for a photonic response. Detecting no photons implies a 'dark' $m_s = \pm 1$ state, and receiving at least one photon implies the 'bright' $m_s = 0$ state. It is important to know and optimise the fidelity of this process, the calibration of which is detailed in Figure 6.3.

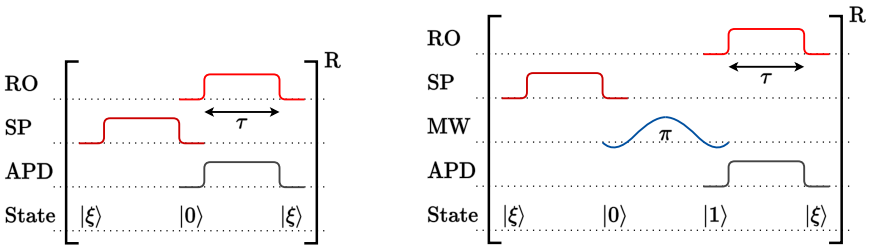

Figure 6.3: *Diagram showing single-short readout (SSRO) calibration procedure, split into bright and dark calibration. (a) Calibration of the bright state readout. The spinpump pulse initialises the state $|0\rangle$. Afterwards, the readout laser is driving while collecting photons in the PSB. This procedure is repeated multiple times to generate the bright fidelity: the probability over time to detect at least one photon. (b) Calibration of the dark state readout. A similar procedure to (a), but after initialisation to $|0\rangle$ the state is now flipped to $|\pm 1\rangle$ using a microwave pi-pulse. Now the fidelity is the probability to detect no photons over time. The optimal readout pulse time is extracted as the time with the highest average fidelity.*

6.1.5 Optical pi-pulse

For entanglement generation, it is crucial to be able to send out single-photons, correlated with the NV spin state. These are ideally generated by instantly flipping the spin state to a bright excited state when in $|0\rangle$, which will decay back to $|0\rangle$ with high probability under emission of a photon. Practically, the challenge is to make the a short pulse with the correct energy to precisely rotate to the excited state. While the discussion of shaping the pulse using AOM and EOM timing is outside the scope of this work, the important part is that the pulse shape is tuned separately, with the remaining parameter the height of the peak. The procedure to optimise the power is detailed in Figure 6.4.

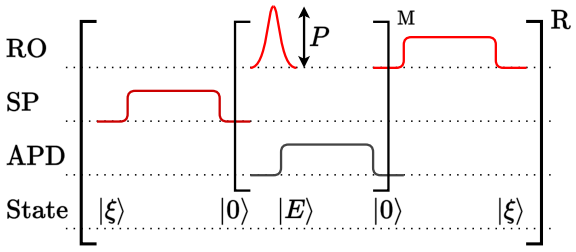

Figure 6.4: *Diagram showing the procedure to calibrate an optical pi-pulse. The spin state is first pumped to the* $|0\rangle$ *state, and excited with the optical pi-pulse, while monitoring the counts in the PSB through the timetagger and integrating the photon counts in the exponential light decay tail after the pulse. This process is repeated multiple times for each optical pi-pulse power and for multiple powers. The power with the highest mean photon count in the tail is selected.*

6.2 Cyclicity model verification

One of the main goals of this thesis project is to verify the predictions made by the cyclicity model presented in Chapter 5. This will be done in a two-pronged approach, as a function of perpendicular strain. Firstly, $|E_{x,y}\rangle$ cyclicity will be measured through mean emitted photon number, and compared to the model's predictions. This should provide a direct check of the model's predictive ability for the states where cyclicity is most crucial. Secondly, the aspect of the model with the largest uncertainty will be verified: the singlet branching ratios. The literature value for the branching ratio out of the singlet states has a notably large uncertainty, while for both branching into and out of the singlet states it is unknown whether a strain dependence is present. These branching ratios will be measured for the $|E_{1,2}\rangle$ state, the results of which can then be fed back into the model for improved accuracy. The two measurements are discussed in detail below

6.2.1 Cyclicity measurements

In the high-cyclicity limit, valid for $|E_{x,y}\rangle$, the cyclicity of a state can be found through its mean number of emitted photons before a spin flip, $\langle n_{\text{photon}}\rangle \approx p_{\text{flip}}$. In practice, where not emitted photons can be detected, this mean emitted photon count can be found through the mean detected photon count before a spin flip, and the probability to detect an emitted photon, $\langle n_{\text{photon}}\rangle = \langle n^{\text{det}}_{\text{photon}}\rangle/\eta^{\text{det}}$. To find the excited state cyclicity, these two values will be measured. The mean detected photon number $\langle n^{\text{det}}_{\text{photon}}\rangle$ can be extracted from the bright part of a single-shot readout calibration, i.e. with the scheme shown in Figure 6.3a. If the readout calibration is performed with sufficient power to fully pump away the state, the state readout is precisely equivalent to cycling one of the $m_s = 0$ transitions and collecting its emitted photons until the state flips. Specifically, the countrate decay curve should follow Figure 6.5c: an exponential decay with possible background, $R(t) = R_0(1 - \exp(-t/\tau))$. The desired photon count signal is found as the area under the exponential decay without background, i.e. $\langle n\rangle = A\tau$. When the same procedure is repeated for the dark state measurement, it can additionally be checked whether the state was fully spinpumped to $|0\rangle$: if an exponential decay is visible in that measurement, the initialisation was likely imperfect.

The more complex measurement is to find the photon detection efficiency η^{det}. A procedure is presented which extracts this value from SSRO calibrations as well, initially presented in [18]. This method applies the fact that the instantaneous photon emission of the excited state population always equals $1/(12.3\text{ ns})$. In case of non-perfect cyclicity the excited state population quickly decays, but the zero-time brightness R_0 remains unaffected. The second crucial realisation is for saturated steady-state driving, always half of state is excited. Hence, we expect a brightness of half the theoretical maximum rate for saturated driving, and we want to

measure this saturation rate: the detection efficiency is the fraction of ideal saturation rate, $\eta = 2R^{\text{det}}_{\text{sat}}/R_{\text{sat}}$. For non-saturated driving powers, the zero-time rate should follow a saturation curve, $R = R_{\text{max}}/(1 + P/P_{\text{sat}})$, see Figure 7.2c. Hence, we can find the saturation rate by performing multiple SSRO calibrations over different readout laser powers, as illustrated in Figure 6.5b, find their zero-time countrates, and fit a saturation curve to the countrate to find the saturate rate and hence the detection efficiency.

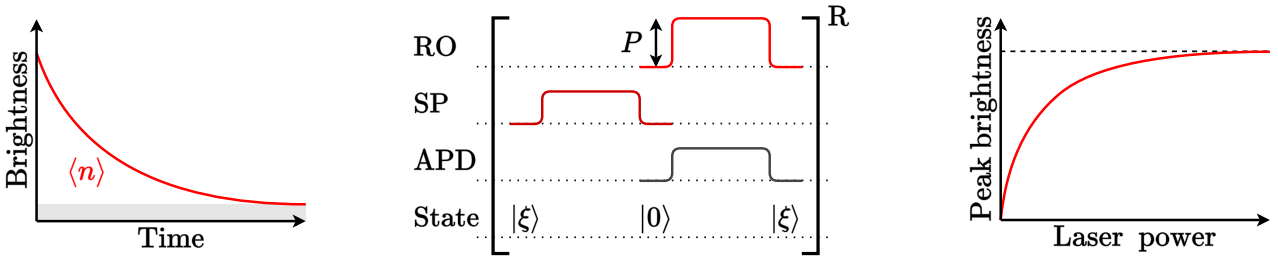

(a) (b) (c)

Figure 6.5: *Mean photon emission figures. (a) Mean NV photon detection profile under constant driving. Fitting an exponential decay with constant background to the curve allow expraction of the mean emitted photon counts, as the surface below the decay curve excluding background. (b) Photon detection efficiency measurement: the countrate decay of the bright state is measured for multiple different readout powers. The instantaneous zero-time countrates should follow a saturation curve. (c) Expected countrate saturation curve, following* $R(P) = R_{sat}/(1 + P/P_{sat})$.

6.2.2 Branching ratio

The branching ratios into and out of the singlet states can be determined by directly measuring the excited state decay rate into the singlet state on one hand, and measuring the total spin-flip probability on the other. The singlet branching ratio out of the singlet state can then indirectly be computed. To measure the branching ratio into the singlet states, we use the fact that the decay rate into the singlet states directly influences the corresponding excited state's lifetime, according to Equation 5.3. The branching ratio into the singlet states can then be computed as $k_{\text{singlet}} = 1 - \tau_{\text{NV}}/\tau_{\text{meas}}$. We can directly measure the excited state lifetime to derive the ratio, using an optical pi calibration: the decay in brightness after an optical pi-pulse is precisely determined by the lifetime of the excited state. To that end, we need to be able to perform and calibrate and optical pi-pulse on a $m_s = \pm 1$ excited state, the process of which is detailed in Figure 6.6a. To measure the excited state lifetime decay, the optical pi-pulse calibration can be rerun at a single (ideally optimal) power for many iterations, such that a single exponential decay curve can be fit to the tail counts.

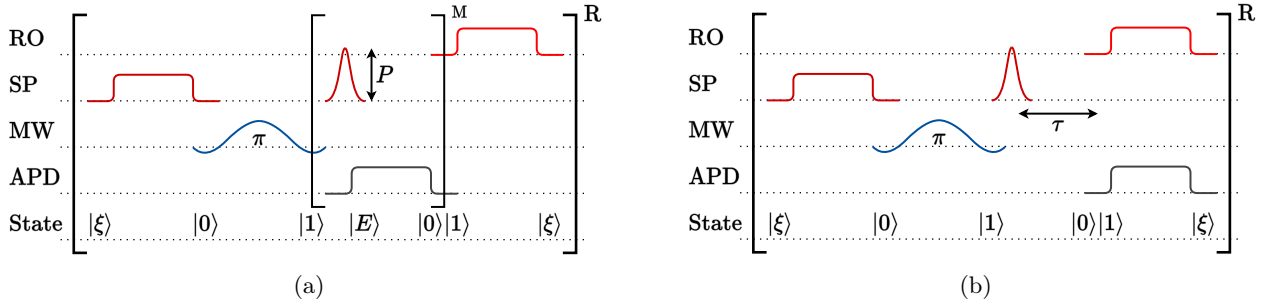

(a) (b)

Figure 6.6: *Singlet branching ratio measurements. (a) Diagram showing the process to perform an optical pi-pulse calibration on a spinpump transition, rather than a readout transition. The process is identical to that shown in Figure 6.4, except for the addition of a microwave pi-pulse before the optical pi-pulse, and the laser on which the optical pi-pulse is performed. Note that the spinpump transitions have a high spin-flip probability, so M must remain low. (b) Spin-flip probability measurement for low cyclicity states. For short* τ *(*$8\text{ ns} \ll \tau \ll 371\text{ ns}$*), it is possible to measure the direct spin-flip probability, while for long* τ *(*$\tau \gg 371\text{ ns}$*) it is possible to extract the total spin-flip probability.*

For branching out of the singlet, we want to measure the net spin-flip probability from $|E_{1,2}\rangle$ to $|0\rangle$. With the branching ratio into the singlet state known from the previous measurement, this immediately gives a value for

for the singlet branching ratio. To actually measure the spin-flip probability, we perform a SSRO calibration, but with a third run where an additional optical pi-pulse is performed between initialising to $|\pm 1\rangle$ and readout, see Figure 6.6b. When performing the readout block long after the optical pi-pulse (i.e. $\tau \gg 371$ ns), this result can be compared to the bounds set by a normal SSRO, to get a direct measure for the net spin-flip probability. To remove the influence of direct $|E_{1,2}\rangle$ to $|0\rangle$, we could additionally measure a short time after the optical pi-pulse (τ (8 ns $\ll \tau \ll$ 371 ns) to also get value for faster direct decay, as done in [27]. This final step is not performed in this work due to time constraints, both in measurement time and implementation time.

7 Results

In this section, the results of the cyclicity model verification are discussed, split by the specific measurements. Firstly, the process and results of strain tuning are discussed. Then, the results of the two measurements towards cyclicity are discussed, that is, the detection efficiency measurement and mean photon number measurements. Finally, the attempts to verify the singlet branching ratios are presented.

All measurements were performed the NV centre in SIL2 of the QLink Demonstrator Node 2. This NV centre has a low naturally occurring perpendicular strain of around 1.0 GHz, which guarantees the ability to reach both low and high strain with DC Stark tuning, and a constant strain angle at high strain regimes. The magnetic field at the sample is measured at $B_z \approx 40$ G, placing the $|\pm 1\rangle$ ground states 2.79 GHz and 2.97 GHz from $|0\rangle$. The cryostat thermometer near the sample indicated a temperature of $T = 9$ K during the measurements, higher than the set value of $T = 4$ K. Finally, the specific sample is known to have a residual layer of chromium left on its surface from manufacturing.

All data was obtained in a single sweep from high to low strain, at the gate voltages [−20, −19, −18, −17, −16, −14, −12, −10, −7.5, −5, −2.5, 0] V. The smaller gate voltage steps at high strain were chosen for improved contrast of mixing effects there. Solely the linescans shown in Figure 7.1a were performed earlier, while moving towards high gate voltage.

7.1 Strain tuning

The perpendicular strain is increased by applying a DC electric field to the sample's microwave stripline, while keeping the gates grounded. The strain increases with the application of a negative voltage, which is measured with linescans down to −10 V, shown in Figure 7.1a. At −10 V, the $|E_{x,y}\rangle$ frequencies lie approximately 11 GHz apart, meaning a strain level of 5.5 GHz and a strain tuning effect of 0.45 GHz/V. No complete linescans were performed for larger gate voltages, due to the large frequency sweep range required of the readout laser. While tuning the gate voltage, the moving resonance peaks are continuously tracked using the CR check feedback mechanism described in Section 6.1.3. Specifically, the gate voltage is changed slowly at 5 mV/s while CR checking on the $|E_y\rangle$ (RO) and $|E_2\rangle$ (SP) lines. These transitions were chosen for their absence of energy crossings over the given domain. The $|E_y\rangle$ resonance frequencies found this way are plotted in Figure 7.1b, as well as occasional deliberate jumps to $|E_x\rangle$ to visually show strain increase with gate voltage.

Unexpectedly, the strain values obtained through linescans and CR checking were observed to diverge for higher gate voltage, shown in Figure 7.1c, with a difference of around 40% percent observed at −10 V. To explain this discrepancy, it is noted that the main difference between linescans and CR checking is the difference in red laser power, at 1 nW and 51 nW, respectively, due to the addition of a spinpump laser field for the latter. To verify whether the laser field is responsible for the line shift, a set of linescans was performed with the addition of an off-resonant spinpump laser field. Indeed, as shown in Figure 7.1d, a shift in $|E_x\rangle$ resonance frequency is observed with increased spinpump laser power. Specifically, the resonance frequency follows a logarithmic shift as function of combined red laser power, as is shown in Figure 7.1e. When the sequence is repeated with the fibre of the spinpump laser disconnected, the frequency shift does not occur, and the effect remains present after deicing the sample. As shown in Figure A.1b and A.1c in the Appendix, the same logarithmic shift is observed with increased readout power and for changing spinpump laser power during CR checking, and the effect is highly time-symmetric. Changing yellow laser power shows a limited effect (not shown), while changing the time between yellow and red laser power shows no effect, see Figure A.1d.

For CR checking during the remainder of the experiments, repumping was performed for 500 µs with 50 nW of yellow laser power, while resonance checking was performed for 50 µs with 50 nW of spinpump laser power, and 1 nW or 2 nW of readout laser power. The readout power was increased at high strain for improved line tracking, as the automated tracking had difficulty tracking the lines for the low cyclicity and hence low photon count observed at higher strain levels.

7.2 Detection efficiency

Photon detection efficiency measurements, as described in Section 6.2.1, were performed at multiple gate voltages. The measurements were performed on the $|E_x\rangle$ and $|E_2\rangle$ transitions for readout and spinpumping, except at −10 V where the $|E_y\rangle$ transition was used for readout due to the $|E_x\rangle$ $|A_1\rangle$ crossing there.

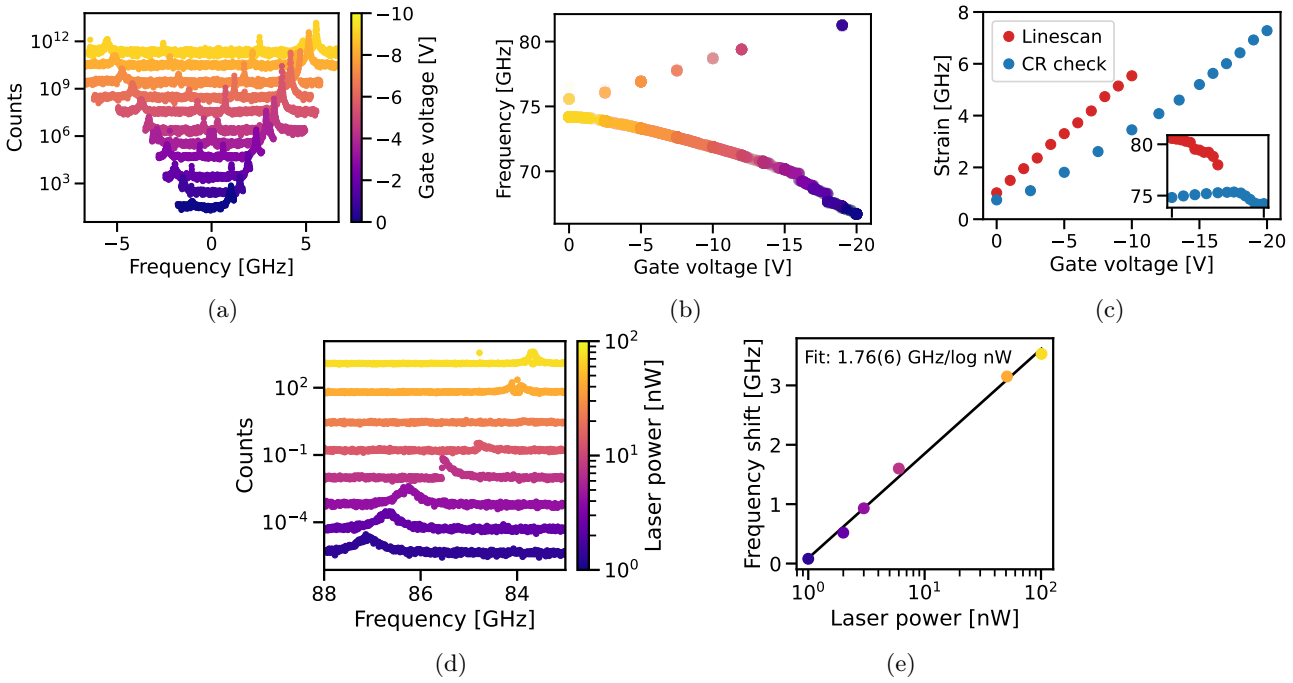

Figure 7.1: *Strain tuning results. Shown frequencies are defined relative to* 470.4 THz *unless states otherwise. (a) Linescans for integer gate voltages up to* −10 V*, performed with* 1 nW *RO and* 50 nW *yellow laser power. Large peaks show the* $|0\rangle \rightarrow |E_{y/x}\rangle$ *transitions of the left/right. The small peaks in the middle are offset from the large peaks by* 3.0 GHz*, corresponding to the continuously driven* $|0\rangle \rightarrow |+1\rangle$ *microwave transition. The parallel strain has been subtracted subtracted from the shown frequencies for readability, and is shown in the inset of (c). (b) CR check resonance over gate voltage during gate voltage tuning at* 5 mV/s*, performed with* 1 nW *RO,* 50 nW *SP and* 50 nW *yellow laser power. Lower line shows* $|E_y\rangle$ *line tracking, upper dots show deliberate jumps to* $|E_x\rangle$ *to show strain increase. Colors represent unique runs. The frequency jumps at gate voltages between* −15 V *and* −20 V *occurred in the time between measurements. (c) Perpendicular strain extracted from the linescans and CR checks shown in (a,b). The inset shows parallel strain over gate voltage, drifted between the two measurements. The CR checking measurements taken alongside the linescans are shown in Figure A.1a in the Appendix, showing parallel strain close to that of the linescans. (d) Linescans showing shifting* $|E_x\rangle$ *resonance frequency when applying off-resonant SP light at different powers, taken at* −20 V*, i.e.* 7.5 GHz *strain. Multiple runs show lost signal halfway through the scan due to charge jumps. Horizontal axis flipped for readability. (e)* $|E_x\rangle$ *resonance frequency as a function of laser power, extracted from (d). Zero point set at* 87.2 GHz *for readability.*

The detection efficiency measurement at 0 V is presented as example. The brightness decay curves obtained in that measurement are shown in Figure 7.2a, showing an increasing exponential decay rate over laser power, but for higher laser powers also a second, unexpected fast decay term on ∼300 ns timescale. This fast term is suspected to be caused by coherent optical driving, and is discussed in detail in the Discussion chapter. For the remainder of this section, the fast decay term is neglected as it violates the steady-state assumption made in the efficiency calculation.

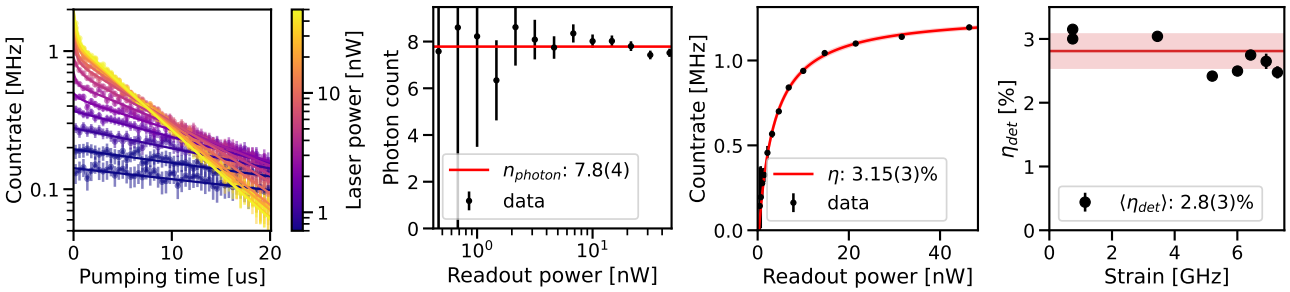

(a) (b) (c) (d)

Figure 7.2: *Detection efficiency measurements. Spinpumping performed for* 50 µs *at* 100 nW*, while readout performed for* 20 µs *and swept between 0.5-*50 nW*. (a) Readout countrate decay over time for varying readout laser power. An additional fast decay term on* 300 ns *timescale is observed but ignored for fitting of the larger timescale exponential decay. Shown data has been rebinned 100-fold for readability. (b) Mean number of detected photons per excitation over laser power, extracted from the fits in (a). (c) Saturation of zero-time countrate over laser power, extracted from decay fits shown in (a). Fit yields* $P_{sat} = 3.5(2)$ nW *and* $R_{sat} = 1.28(1)$ MHz*. Legend shows photon detection efficiency extracted from saturation rate. (d) Photon detection efficiencies measured at different strain levels. A slight decrease in efficiency is observed over strain, see main text. The values in (a-c) correspond to the upper lowest-strain data point.*

The mean photon count per excitation, $\langle n_{\text{photon}}^{\text{det}} \rangle$, and the instantaneous countrate at $t = 0$, R_0, are extracted from the decay curves, and shown in Figures 7.2b and 7.2c, respectively. The shown photon count shows an approximately constant value over laser power, while the countrate shows a saturation curve over laser power. A fit to the latter curve yields a detection efficiency value according to Equation [EQUATION]. The detection efficiency values measured at all different strain levels are shown in Figure 7.2d, yielding a mean detection efficiency of $\eta_{det} = 2.8(3)\%$ with individual values ranging between 3.2% and 2.4% for lower and higher strain, respectively.

The lower fitted detection efficiency values at high strain correspond with a decrease in fitted photon counts and countrate at higher laser power there, see Figure A.2 in the Appendix. This will be discussed in detail in the next chapter. For the remainder of this section, however, the obtained mean value $\eta_{det} = 2.8(3)\%$ is used.

7.3 Photon count

Mean photon count measurements were performed at all gate voltage steps for both the $|E_x\rangle$ and $|E_y\rangle$. The mean detected photon counts, $\langle n_{\text{photon}}^{\text{det}} \rangle$, were obtained by the same fitting method as used for the detection efficiency, and the values are shown in Figure 7.3a; both with and without background counts included in the total photon count, and plotted over model predictions for measured temperature, magnetic field and detection efficiency.

The dip in measured $|E_x\rangle$ photon count and increase in its background count around 3.5 GHz strain is caused by the crossing of the $|0\rangle \rightarrow |E_x\rangle$ and $|\pm 1\rangle \rightarrow |A_1\rangle$ transitions. There, the effective noise floor is increased and counts with background included serve as an upper bound of true photon count. Furthermore, for all strain values except 3.5 GHz, the mean counts of $|E_x\rangle$ exceed that of $|E_y\rangle$, while closely approaching each other towards zero strain.

The decrease in countrate for both $|E_x\rangle$ and $|E_y\rangle$ towards 7.5 GHz strain and the consistently higher countrate for $|E_x\rangle$ compared to $|E_y\rangle$ are consistent with model predictions. However, significant discrepancies are observed between predictions and measured values. Firstly, as mentioned in Section 5.6, the model does not take into account the $|E_x\rangle$ transition overlap around 3.5 GHz. Not expected, however, are other discrepancies: the predicted photon counts near zero strain are significantly higher than observed, and between 1 GHz and 6 GHz the measured $|E_x\rangle$ counts are significantly lower than predicted, while $|E_y\rangle$ counts are significantly higher

than predicted. Only above 6 GHz do the measured photon counts fall within the range of predicted values.

Excited state cyclicity $1 - p_{\text{flip}}$ is computed from the mean photon counts using the measured detection efficiency under high cyclicity assumption, and are shown in Figure 7.3b together with model predictions given the measured input parameters. The same prediction discrepancies are found, as the data is effectively equivalent. Attempts to improve model overlap were made by tuning the detection efficiency or sample temperature fed into the model. The results are shown in Figure A.3 in the Appendix, though no significant improvement is observed.

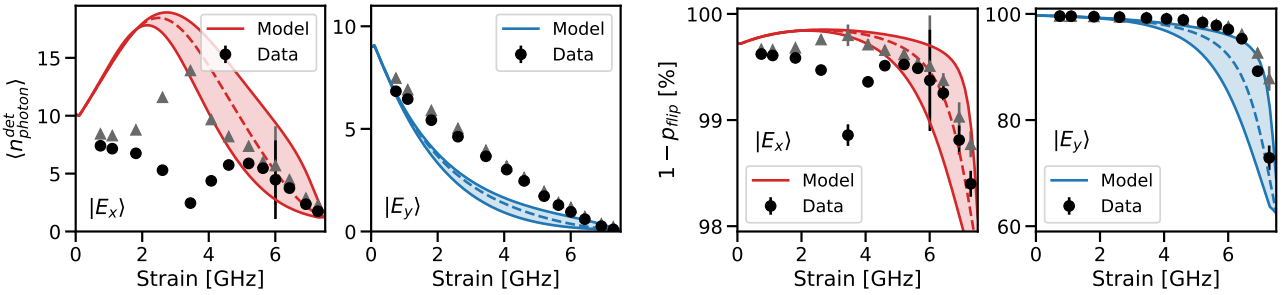

(a) (b)

Figure 7.3: *Measured versus predicted mean photon counts and cyclicities over perpendicular for* $|E_x\rangle$ *and* $|E_y\rangle$*. Readout was performed at* 5 nW *for* 20 ns*, and spinpumping was performed at* 100 nW *for* 50 ns*. The readout power was chosen to give good saturation without significant fast decay peak. (a) Measured and predicted mean photon counts* $\langle n_{photon}^{det} \rangle$*. Black circles show net photon count, while grey triangles show counts including background. The model shows the range of predicted photon count values given the measured values* $\eta_{det} = 2.8(3)\%$*,* $T = 9$ K *and* $B_z = 40$ *G over all possible strain angles* θ*, with the dotted line highlighting the halfway value* $\theta = 20°$*. The dip in photon count and increase in background rate for* $|E_x\rangle$ *corresponds with the crossing between* $|0\rangle \rightarrow |E_x\rangle$ *and* $|\pm 1\rangle \rightarrow |A_1\rangle$ *transitions, which is not simulated in the model. The large* $|E_x\rangle$ *error bar at* 6 GHz *is due to an incomplete spinpump initialisation to* $|0\rangle$*. (b) Measured and predicted cyclicities* $1 - p_{flip}$*. Measured values use* $\eta_{det} = 2.8(3)\%$ *to compute cyclicity. Further description equivalent to (a).*

7.4 Singlet branching ratio

The branching ratios into the singlet states and the total spin-flip probabilities were measured for $|E_{1,2}\rangle$ at strain between 5.5-7.5 GHz. Firstly the branching ratio *into* the singlet states is discussed, and secondly the branching ratio *out* of the singlet states.

To derive the excited state decay rate into the singlet states, the excited state lifetimes are measured from the luminescence tail after an optical pi-pulse. An example comparing the lifetime of the $|E_2\rangle$ and $|E_x\rangle$ states at 7.5 GHz is shown in Figure 7.4a. It shows a significantly shorter lifetime for $|E_2\rangle$, indicating that the state indeed retains singlet decay at this strain level. Note that compared to zero strain, the $|E_x\rangle$ lifetime is shorter while the $|E_2\rangle$ lifetime is longer, indicating mixing as predicted by the cyclicity model. The lifetime measurements are repeated for $|E_{1,2}\rangle$ over the strain range 5.5-7.5 GHz, shown in Figure 7.4b. Lifetimes between 7-10 ns are observed, showing consistent nonzero singlet decay.

The branching ratios into the singlet state computed from the excited state lifetimes are shown in Figure 7.4d. Comparing these values to model predictions, shown in 7.4c, show that the spread of computed singlet ratio values is larger than the contrast in predicted values, making verification of the predictions impossible. The large spread of the fitted decay rates was caused by the difficulty to perform good optical pi-pulses during the measurement period, and their low rate at high strain. Consequently, little decay light was available for many of the data points; see Figure A.4a in the Appendix for examples. The challenge surrounding good optical pi-pulses is discussed on page 41.

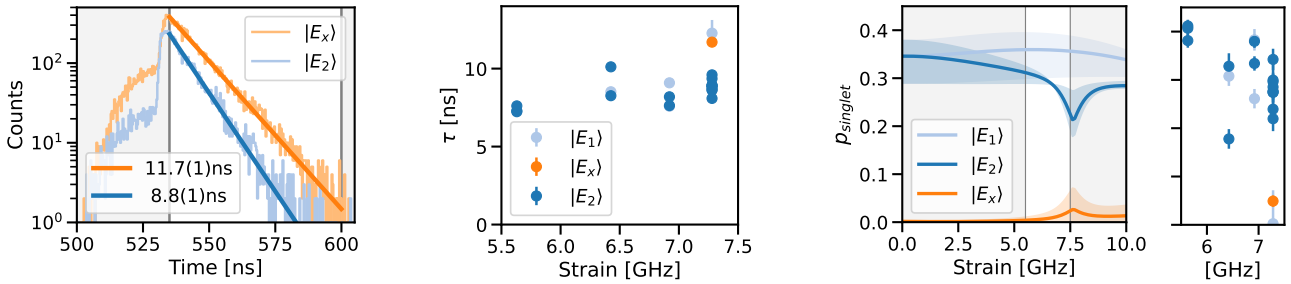

(a) (b) (c) (d)

Figure 7.4: *Excited decay into the singlet states. (a) Example of $|E_x\rangle$ and $|E_2\rangle$ decay at 7.5 GHz strain, showing the shorter lifetime of the latter. (b) Fitted excited state lifetimes over gate voltage, showing lower lifetimes for $|E_{1,2}\rangle$ compared to $|E_x\rangle$. (c) Predicted singlet branching ratio over strain at $T = 12$ K. Bands around prediction indicate temperature range $T = 0 - 20$ K. Highlighted strain band indicates strain range of measurements. (d) Singlet branching ratios computed from excited state lifetimes shown in (b).*

Secondly, an example of a total spin-flip probability measurement is shown in Figure 7.5a. The stabilisation of the ratio indicates a valid measurement approach. However, repeated measurements at different strain levels, shown in Figure 7.5c, show a large spread in values. Moreover, comparison to the predicted values, shown in Figure 7.5b, again shows the spread to exceed the prediction contrast. Hence, the measurements were discontinued below 5.5 GHz strain. Additionally, the values obtained were not deemed sufficient to attempt the computation of singlet-to-ground branching ratios over strain.

The inconsistent measurement outcomes were traced back to a highly fluctuating power of the readout laser. Its spread of maximum powers after each calibration during the measurement period is visualised in Figure 7.5d, showing power fluctuations of a factor of five. These fluctuations were caused by the laser's first AOM, showing a polarisation extinction ratio of only 7dB. This caused the effective power fluctuations due to polarisation filtering downstream, and occurred on the scale of minutes. The precise laser power has a direct impact on an optical pi rotation, meaning that constant power is crucial for the shown measurements. Instead, the laser power changes would occur on a time scale significantly shorter than the optical pi-pulse calibrations or spin-flip probability measurements. Moreover, due to laser calibrations being performed between calibrations and measurements, the actual power during a measurement could both be above or below its target by up to a factor of five.

A final note is made on the spin-flip probabilities found for $|E_1\rangle$, which, despite the large spread in values, show significantly lower spin-flip probabilities than the values obtained for $|E_1\rangle$. This is attributed to an incomplete saturation of the transition, see Figures A.4d through A.4f in the Appendix.

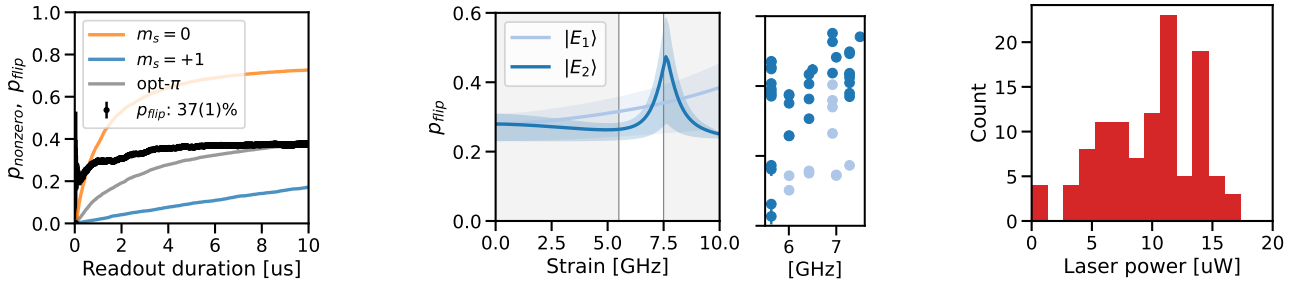

(a) (b) (c) (d)

Figure 7.5: *Singlet-to-ground branching ratio measurements. (a) Single branching ratio measurement, showing a converging spin-flip probability value for larger time. The value shown in the legend is taken that the point of highest fidelity readout, $t = 7$ µs. (b,c) Predicted and extracted spin-flip probabilities over strain. The highlighted band in the predictions shows the measurement strain range. The measured p_{flip} values show a large spread. (d) Observed readout laser powers after each calibration over the measurement period, showing fluctuations of a factor of five.*

8 Discussion and Conclusions

In this chapter, the data presented in Chapter 7 is discussed and interpreted, including future recommendations and conclusions. Each measurement sequence will be discussed separately, as they contain largely separate discussions.

Before discussing the specific measurements, a note is made about the difficulty of yellow CR checking at high strain. Specifically, the low cyclicity there reduces the mean photon count from 40 to around 2 photons per resonance check, at which level distinguishing between resonance counts and noise becomes difficult. This creates two issues. Firstly, the passing rate is reduced by multiple orders magnitude, as the hard CR check threshold needs to remain at around 5 counts to prevent noise counts from initiating a measurement sequence. Secondly, the resonance linetracking algorithm becomes unreliable, as it can veer away from the resonance frequency due to noise counts. This requires constant attention from the operator. While the shot noise is inherent at low cyclicity, a more accurate linetracking method exists which tunes the gate voltage instead of the laser frequencies [31]. For repeated measurements at high strain and electric field, such a linetracking method is highly advised.

8.1 Strain tuning

Strain tuning was successfully performed in this work through DC Stark tuning, with a strain change from 1.0 GHz to 7.5 GHz observed over a gate voltage range of -20 V. An unexpected effect was observed while strain tuning: a logarithmic decrease in effective strain with increased laser power. To the best of the author's knowledge, this effect has not been observed before in literature, though common NV centre operations would not show the shifts. A similar shift has been observed with green laser power, though at three orders of magnitude more power [30].

As the resonance frequency shifts did not present themselves at zero gate voltage, it is concluded that the laser field affects the effective applied electric field. Electromagnetic interference and ice are discarded as causes, as blocking the laser light negates the effect and regularly deicing were performed. Sample heating is additionally discarded as cause due to the low laser powers at which the frequency shifts occur.

No laser frequency dependence of the resonance shifts was found, with the effect observed for different red optical frequencies and yellow optical field. Although the timescale of the effect is not known, an upper and lower bound can be extracted. As NV experiments are still possible, the effect must be significantly slower than microsecond scale. Conversely, the effect must be faster than second scale, as frequency shifts are visually instant when changing laser powers by hand.

The residual layer of chromium left on the sample after manufacturing is proposed as a possible cause for the effect. This layer may facilitate conduction of current under illumination and thus lower the local electric field, although no physical justification could be found for this phenomenon. An attempt to measure the consequent leakage current to ground was inconclusive. The current meter indicated the current below its lower threshold of 100 nA, though a more rigorous measurement is advised for a decisive answer.

Crucially, it is advised to investigate the reproducibility of the frequency shifts in other NV centres in the same diamond, and if so, investigate whether the effect is reproducible in other diamonds and/or setups. The latter is proposed to be performed on one of the nodes used in e.g. [31]. Results of that measurement should narrow the investigation space.

8.2 Detection efficiency

Successful detection efficiency measurements were performed over the complete strain range, giving a weighted mean value of $\eta_{det} = 2.8(3)\%$. However, in the readout countrate decay curves, an unexpected second decay term is observed with lifetime $\sim$ 300ns. For the detection efficiency fitting, this term was ignored. At higher strain level, a decrease in photon counts and peak fitted countrate was additionally observed, giving a slight decrease in detection efficiency from 3.1% to 2.5%. This section will discuss the interpretation of the fast decay term, the validity of ignoring this term, and possible relation to the drop in detection efficiency.

Increased laser power and detection artefacts are discarded as causes of the fast decay term, respectively, by checking reflection off the stripline and by logical argument that the latter would decrease counts instead

of raising them. Instead, the fast decay term is suspected to be caused by initial coherent state driving at low time, with a large portion of the state being pushed to the excited state before dephasing to steady-state behaviour through the singlet states. This theory is supported by the fact that it is only observed at higher laser power, that the amplitude of the fast decay peak never significantly exceeds the amplitude of the slow decay, and that fast decay occurs on the time order of the singlet lifetime. It is advised to validate this theory with a simulation of the state evolution over time, by writing and solving the decay master equations in Lindblad form.

Assuming the fast decay is indeed caused by coherent behaviour, it breaks the steady-state assumption made in the detection efficiency calculation, and hence the peak should be ignored for fitting. This has no significant impact on fitted peak countrate, as long as the number of photons in the fast decay is negligible. However, fitting of a double exponential curve to the highest laser power decay curves of each measurement shows that 3% to 20% of total photon counts are found in the fast decay peak for low to high strain. This is not negligible for high strain, and, moreover, is strongly correlated to the high-strain drop in photon counts, peak countrate and detection efficiency. If simulations would show the effect to indeed be caused by coherent driving, a more elaborate fitting algorithm could be implemented to compensate for the counts lost in the the fast decay.

8.3 Cyclicity

Mean photon counts $\langle n_{\text{photon}}^{\text{det}} \rangle$ were successfully measured for both $|E_x\rangle$ and $|E_y\rangle$, over a perpendicular strain range up to 7.5 GHz, showing a decrease towards higher strain. Furthermore, the state cyclicities $1 - p_{\text{flip}}$ were derived using measured detection efficiency. However, the attempted verification of the cyclicity model shows significant unexpected discrepancies between model predictions and measured values. This section will discuss the discrepancies in two areas, towards zero strain and up to around 6 GHz, and finally discusses next steps.

Firstly, towards zero strain, the model predicts a convergence of $|E_{x,y}\rangle$ photon counts toward a value that is only influenced externally by the photon detection efficiency. The photon detection efficiency was explicitly measured in this work at $\eta_{det} = 2.8(3)\%$, which should yield a good prediction for photon counts in the zero-strain limit of 9-10 photons. Yet, the measured photon counts for both $|E_x\rangle$ and $|E_y\rangle$ appear to approach 7-8 counts at zero strain. Most constants fed into the cyclicity were precisely researched at this low strain level, making this discrepancy unexpected. It may suggest an overestimation of the detection efficiency, or a singlet branching ratio more in favour to $|\pm 1\rangle$, though many parameters could be changed to give a lower predicted count.

Secondly, at nonzero strain below approximately 6 GHz, the model predicts significantly higher counts for $|E_x\rangle$ but lower counts for $|E_y\rangle$, and a different shape in photon count decrease for $|E_y\rangle$ all together. This may suggest stronger temperature mixing is taking place between $|E_{x,y}\rangle$ in this regime, as that would pull the counts closer together. However, again multiple parameters could cause the difference.

Crucially, the focus of the cyclicity model's development was on excited state behaviour at a temperature of $T = 4$K where temperature effects are almost negligible, and therefore the implementation of temperature mixing is only approximate. The uncertainty this creates prevents drawing any hard conclusions on model performance. To allow for proper validation, it is advised to repeat the measurements in experimental conditions closer to the model's native approach, or implement a more accurate temperature mixing model.

8.4 Singlet branching

Although a framework for singlet branching measurements was successfully established, both excited state lifetime measurements and singlet-to-ground branching ratio measurements were limited by bad optical pi-pulses. The limited conclusions and discussions of both measurements are treated separately.

For the excited state lifetime measurements, inconsistent optical pi-pulses should not have an effect on the lifetime of the excited state, meaning that the measurements should in principle be valid despite the readout laser's inconsistent power. The low photon count caused by the inconsistent optical pi-pulses, however, severely limits the fitting accuracy. The couple good runs highlighted in the main text section do show promise, and clearly show that the $|E_{1,2}\rangle$ states maintain significant singlet branching at higher strain levels. For any comparison to the model predictions though, repetition of the measurements with more photon counts is required, and over a larger strain range for a full comparison.

A similar story holds for the total spin-flip probability measurements, which would ideally give values for

the singlet-to-ground branching ratio. The measurement framework appears valid given a good optical pi-pulse, and $|E_2\rangle$ results show continued high branching to $|0\rangle$ at high strain, but with the spread far exceeding the contrast. Before redoing the measurements with stable laser power, it advised to investigate the feasibility to implement the full scheme by [27], that is, with multiple shorter readouts after the optical pi-pulse, such that an inherent distinction can be obtained between direct and singlet decay. With the current measurement framework, the singlet branching ratio needs to be extracted implicitly, which increases errors and limits interpretation. It should be noted, however, that a full time-sweep measurement will be very slow at low cyclicity. It should first be investigated whether the measurement is feasible time-wise.

References

[1] S. Wehner, D. Elkouss, and R. Hanson, "Quantum internet: A vision for the road ahead," Science, vol. 362, 10 2018.

[2] A. Teepe, Two-Photon Quantum Interference using a Single Nitrogen-Vacancy Center (MSc thesis). Delft University of Technology, 2021.

[3] F. Jelezko and J. Wrachtrup, "Single defect centres in diamond: A review," physica status solidi (a), vol. 203, pp. 3207–3225, 10 2006.

[4] M. W. Doherty, N. B. Manson, P. Delaney, F. Jelezko, J. Wrachtrup, and L. C. Hollenberg, "The nitrogen-vacancy colour centre in diamond," Physics Reports, vol. 528, pp. 1–45, 7 2013.

[5] W. Pfaff, Quantum measurement and entanglement of spin quantum bits in diamond (PhD thesis). Delft University of Technology, 2013.

[6] M. Teng, Towards entanglement generation between nitrogen vacancy centres in diamond over metropolitan distances t Delft University of Technology, 2019.

[7] T. Van der Sar, Quantum control of single spins and single photons in diamond (PhD thesis). Delft University of Technology, 2012.

[8] S. Faes, Preparing Quantum Interference of Two to Telecom Wavelength Converted Single Photons Emitted by NV Cer Delft University of Technology, 2020.

[9] B. Hensen, H. Bernien, A. E. Dréau, A. Reiserer, N. Kalb, M. S. Blok, J. Ruitenberg, R. F. L. Vermeulen, R. N. Schouten, C. Abellán, W. Amaya, V. Pruneri, M. W. Mitchell, M. Markham, D. J. Twitchen, D. Elkouss, S. Wehner, T. H. Taminiau, and R. Hanson, "Loophole-free Bell inequality violation using electron spins separated by 1.3 kilometres," Nature 2015 526:7575, vol. 526, pp. 682–686, 10 2015.

[10] A. Dréau, A. Tchebotareva, A. E. Mahdaoui, C. Bonato, and R. Hanson, "Quantum Frequency Conversion of Single Photons from a Nitrogen-Vacancy Center in Diamond to Telecommunication Wavelengths," Physical Review Applied, vol. 9, p. 064031, 6 2018.

[11] A. Tchebotareva, S. L. N. Hermans, P. C. Humphreys, D. Voigt, P. J. Harmsma, L. K. Cheng, A. L. Verlaan, N. Dijkhuizen, W. De Jong, A. Dréau, and R. Hanson, "Entanglement between a Diamond Spin Qubit and a Photonic Time-Bin Qubit at Telecom Wavelength," Physical Review Letters, vol. 123, 2019.

[12] C. Cabrillo, J. I. Cirac, P. García-Fernández, and P. Zoller, "Creation of entangled states of distant atoms by interference," Physical Review A, vol. 59, p. 1025, 2 1999.

[13] S. D. Barrett and P. Kok, "Efficient high-fidelity quantum computation using matter qubits and linear optics," Physical Review A, vol. 71, p. 060310, 6 2005.

[14] C. K. Hong, Z. Y. Ou, and L. Mandel, "Measurement of subpicosecond time intervals between two photons by interference," Physical Review Letters, vol. 59, p. 2044, 11 1987.

[15] A. J. Stolk, K. L. van der Enden, M. C. Röhsner, A. Teepe, S. Faes, S. Cadot, J. van Rantwijk, R. Hagen, A. Verlaan, B. Biemond, A. Khorev, R. Vollmer, J. Morits, E. van Zwet, K. J. de Kraker, and R. Hanson, "Telecom-band quantum interference of frequency-converted photons from remote detuned NV centers," (in preparation), 2022.

[16] H. Bernien, Control, measurement and entanglement of remote quantum spin registers in diamond (PhD thesis). Delft University of Technology, 2014.

[17] L. Robledo, L. Childress, H. Bernien, B. Hensen, P. F. A. Alkemade, and R. Hanson, "High-fidelity projective read-out of a solid-state spin quantum register," Nature 2011 477:7366, vol. 477, pp. 574–578, 9 2011.

[18] B. J. Hensen, Measurement-based Quantum Computation with the Nitrogen-Vacancy centre in Diamond. PhD thesis, Delft University of Technology, Delft, 2011.

[19] M. L. Goldman, A. Sipahigil, M. W. Doherty, N. Y. Yao, S. D. Bennett, M. Markham, D. J. Twitchen, N. B. Manson, A. Kubanek, and M. D. Lukin, "Phonon-Induced Population Dynamics and Intersystem Crossing in Nitrogen-Vacancy Centers," 2015.

[20] H. K. C. Beukers, Improving coherence of quantum memory during entanglement creation between nitrogen vacancy ce PhD thesis, University of Groningen, Delft Univeristy of Technology, Delft, 2 2019.

[21] A. Batalov, V. Jacques, F. Kaiser, P. Siyushev, P. Neumann, L. J. Rogers, R. L. McMurtrie, N. B. Manson, F. Jelezko, and J. Wrachtrup, "Low Temperature Studies of the Excited-State Structure of Negatively Charged Nitrogen-Vacancy Color Centers in Diamond," Physical Review Letters, vol. 102, p. 195506, 5 2009.

[22] P. Tamarat, N. B. Manson, J. P. Harrison, R. L. McMurtrie, A. Nizovtsev, C. Santori, R. G. Beausoleil, P. Neumann, T. Gaebel, F. Jelezko, P. Hemmer, and J. Wrachtrup, "Spin-flip and spin-conserving optical transitions of the nitrogen-vacancy centre in diamond," New Journal of Physics, vol. 10, p. 045004, 4 2008.

[23] L. J. Rogers, R. L. McMurtrie, M. J. Sellars, and N. B. Manson, "Time-averaging within the excited state of the nitrogen-vacancy centre in diamond," New Journal of Physics, vol. 11, p. 063007, 6 2009.

[24] N. R. Reddy, N. B. Manson, and E. R. Krausz, "Two-laser spectral hole burning in a colour centre in diamond," Journal of Luminescence, vol. 38, pp. 46–47, 12 1987.

[25] T. Mittiga, S. Hsieh, C. Zu, B. Kobrin, F. Machado, P. Bhattacharyya, N. Z. Rui, A. Jarmola, S. Choi, D. Budker, and N. Y. Yao, "Imaging the Local Charge Environment of Nitrogen-Vacancy Centers in Diamond," Physical Review Letters, vol. 121, p. 246402, 2018.

[26] G. D. Fuchs, V. V. Dobrovitski, R. Hanson, A. Batra, C. D. Weis, T. Schenkel, and D. D. Awschalom, "Excited-State Spectroscopy Using Single Spin Manipulation in Diamond," 2008.

[27] N. Kalb, P. C. Humphreys, J. J. Slim, and R. Hanson, "Dephasing mechanisms of diamond-based nuclear-spin memories for quantum networks," Physical Review A, vol. 97, p. 062330, 6 2018.

[28] L. Robledo, H. Bernien, T. V. D. Sar, and R. Hanson, "Spin dynamics in the optical cycle of single nitrogen-vacancy centres in diamond," New Journal of Physics, vol. 13, p. 025013, 2 2011.

[29] K. M. C. Fu, C. Santori, P. E. Barclay, L. J. Rogers, N. B. Manson, and R. G. Beausoleil, "Observation of the dynamic Jahn-Teller effect in the excited states of nitrogen-vacancy centers in diamond," Physical Review Letters, vol. 103, p. 256404, 12 2009.

[30] L. C. Bassett, F. J. Heremans, C. G. Yale, B. B. Buckley, and D. D. Awschalom, "Electrical Tuning of Single Nitrogen-Vacancy Center Optical Transitions Enhanced by Photoinduced Fields," 4 2011.

[31] M. Pompili, S. L. Hermans, S. Baier, H. K. Beukers, P. C. Humphreys, R. N. Schouten, R. F. Vermeulen, M. J. Tiggelman, L. dos Santos Martins, B. Dirkse, S. Wehner, and R. Hanson, "Realization of a multinode quantum network of remote solid-state qubits," Science, vol. 372, pp. 259–264, 4 2021.

A Appendix A

Supporting material for the Results section.

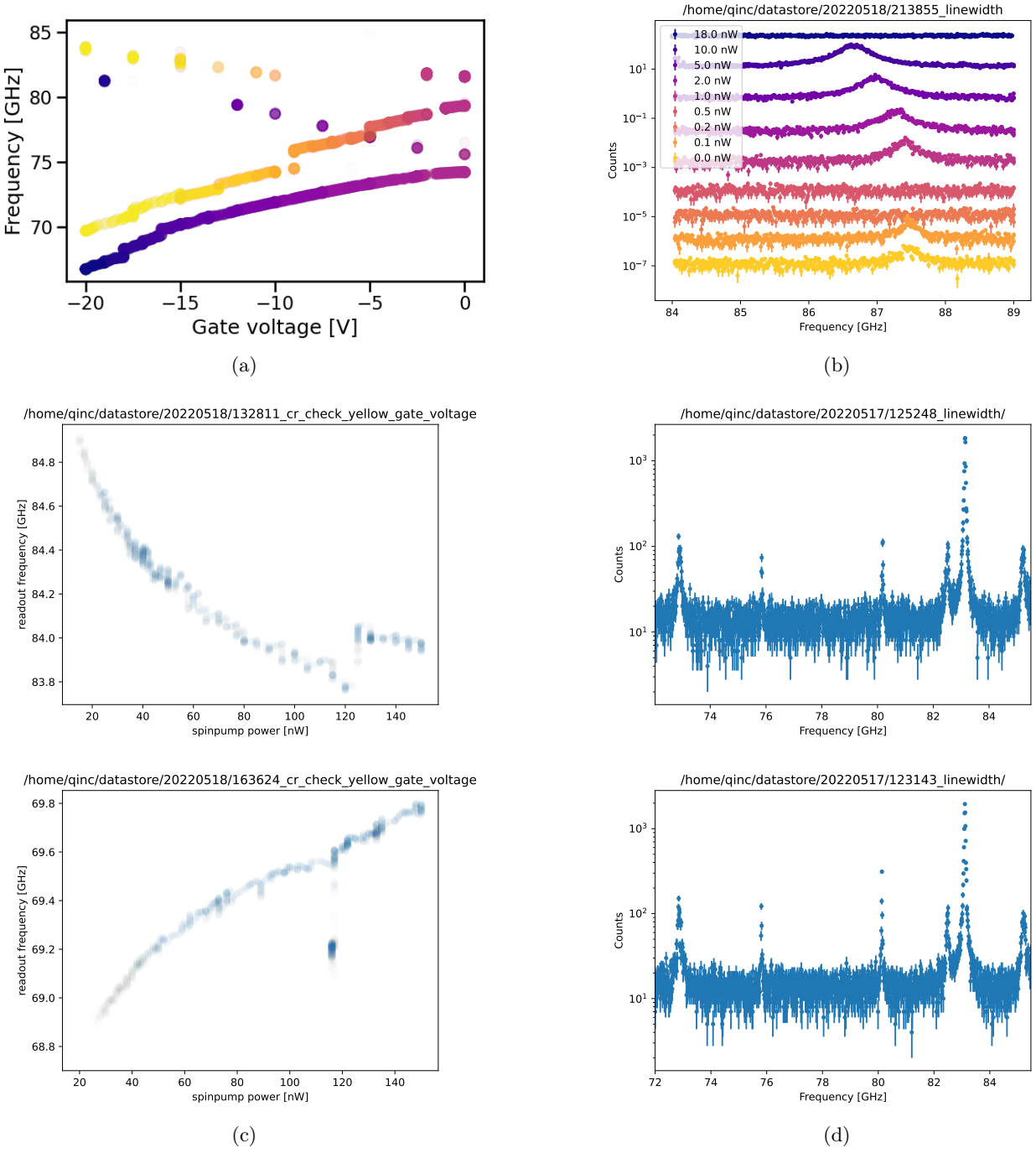

Figure A.1: *Additional strain tuning results. (a) $|E_y\rangle$ (solid) and $|E_x\rangle$ (dots) resonance frequencies over gate voltage, obtained when moving towards higher gate voltage (light colours), compared to the resonance frequencies when moving back to zero electric field (dark colours). Multiple charge jumps are observed, and perpendicular strain has drifted in the three weeks between the measurements. (b) Shift in $|E_x\rangle$ transition frequency as a function of readout laser power, performed at $-20\,\mathrm{V}$. No spinpump laser was applied during the measurement. (c) Shift in $|E_x\rangle$ (top) and $|E_y\rangle$ (bottom) resonance frequencies when changing spinpump laser power, observed with CR checking. Runs performed sequentially, at $-20\,\mathrm{V}$. A charge jump is observed around $120\,\mathrm{nW}$ for both measurements. (d) Linescans applying different waiting times of $10\,\mu\mathrm{s}$ and $50\,\mu\mathrm{s}$ between the yellow and red laser light, showing no line shift. An additional, partial run was performed with $2\,\mu\mathrm{s}$, showing no change either. Sweeps performed at $-9\,\mathrm{V}$.*

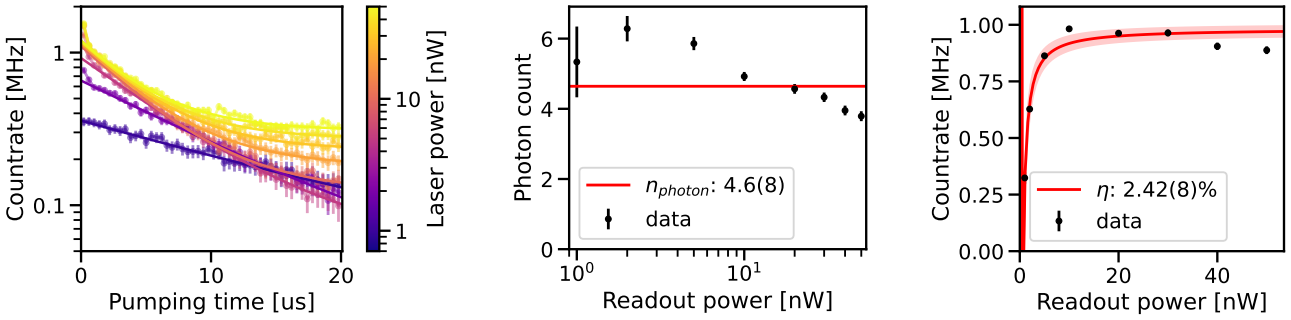

(a) (b) (c)

Figure A.2: *Additional detection efficiency results, showing the results of a non ideal detection efficiency measurement at low strain. (a) Countrate decay curves for a high-strain measurement, showing a significant background rate increase for higher laser powers. (b) Mean photon count fitted to data in (a), showing a 40% decrease in fitted photon count over laser power. (c) Saturation brightness extracted from (a), showing a decrease in peak rate for higher powers, yielding a fitted detection efficiency lower than the countrate found at* 10 nW.

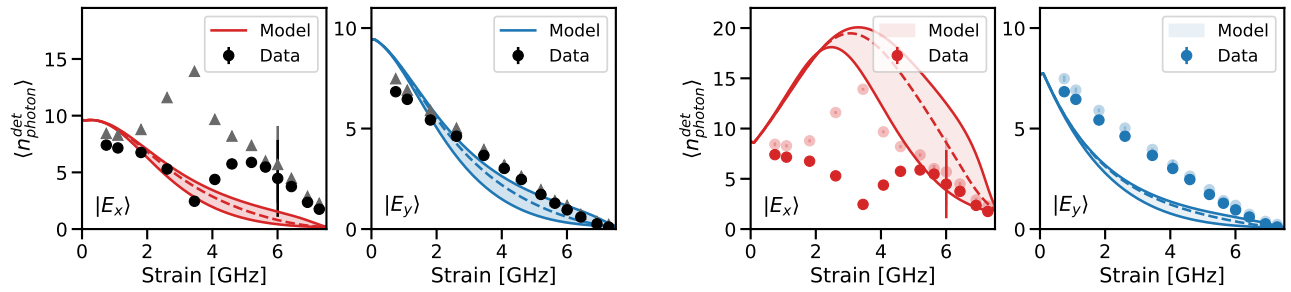

(a) (b)

Figure A.3: *Additional cyclicity comparisons to model predictions. Measurement data identical to main text. (a) Model prediction at higher temperature, with parameters* $\eta = 2.8\%$, $T = 20$ K *and* $B_z = 40$ *G. (b) Model prediction at lower detection efficiency, i.e. with parameters* $\eta = 2.4\%$, $T = 9$ K *and* $B_z = 40$ *G.*

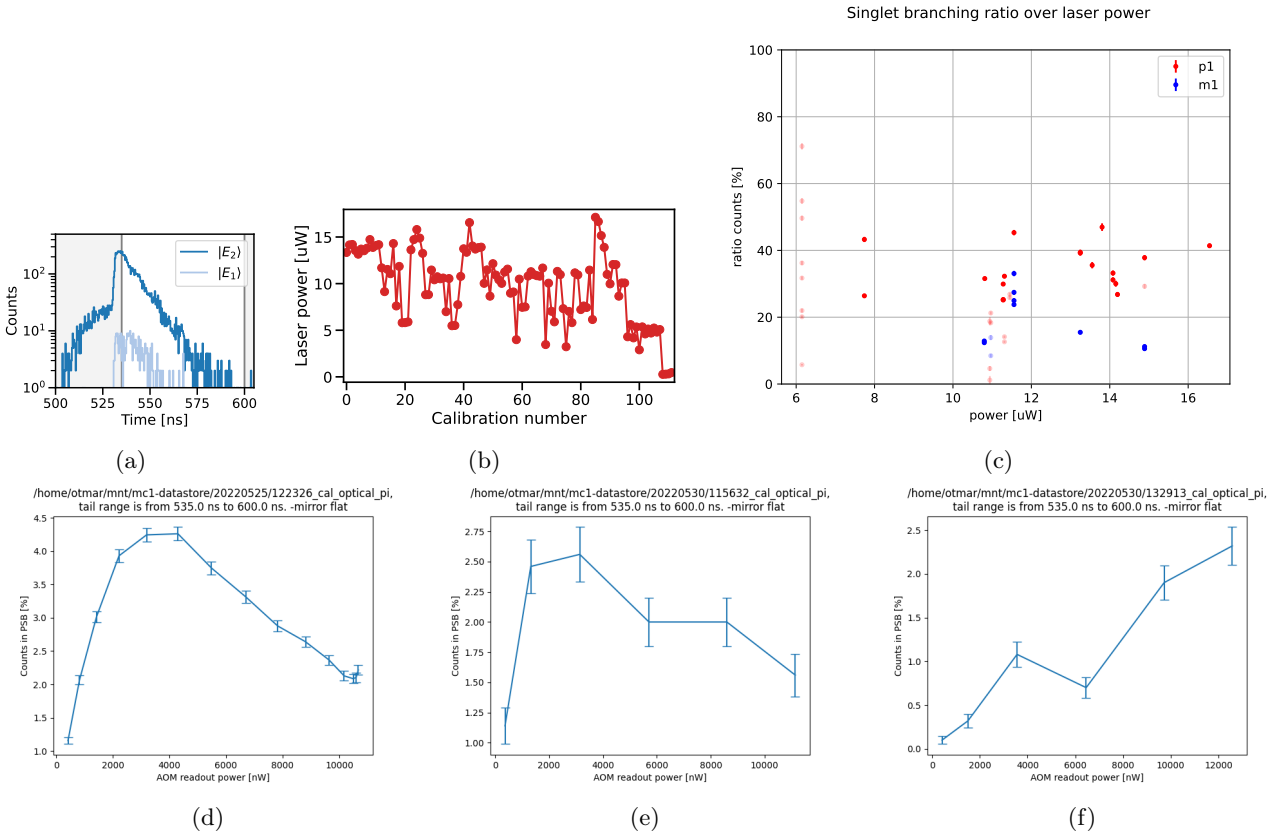

Figure A.4: *Additional singlet ratio figures. (a) Example of excited decay time measurement with low photon count ($|E_1\rangle$), compared to the $|E_2\rangle$ decay curve shown in the main text. (b) Readout laser power after each calibration, showing the power often jumping between calibrations. The measurements were taken over the period of four days. (c) $|E_{1,2}\rangle$ spin-flip probability as a function of the readout laser power found during its last readout calibration, showing no clear correlation. (d,e,f) Examples of optical pi-pulse calibrations for $|E_x\rangle$, $|E_2\rangle$, $|E_1\rangle$. The first shows a well behaved curve, the second as well, although often jumping over the calibration process, and the third never saturating.*

Acknowledgements

It is a pleasure to thank all the great people who have taught and helped me so much over the last ten months, both professionally and socially.

First of course my daily supervisor **Kian**, for which the term 'daily' was certainly not an understatement. I truly could not have wished for a better supervisor over this period. At all times it was clear that you invested 110% in both me and a good project course *for* me, which was definitely not always a given. The long hours in the lab including some unreasonably late nights will be cherished, and I hope I have been able to pay back some of your investment in productive work, unproductive memes and professional-ish photos. Awesome to see you moving up as a Face of Science, and the best of luck with your very own house and managing-director-backed future startup!

And of course the other 'strators: **Arian**, your positive attitude and sense of humour have always been a delight, and your work ethic and vast knowledge impressive. **Marie-Christine**, I do not see how this team could function without your solid mentality and planning skills, and congratulations still on your engagement! Thanks as well for allowing my research to steamroll the Strators meeting for a couple of weeks in a row. The best of luck with the final stretch towards local and long-distance entanglement, I can't wait to see it on every front page!

Ronald, it was an honour to join along in your group. The amazingly supportive and productive environment you have managed to create will be an inspiration and benchmark for years to come. Especially your '~~problem~~ *challenge*' mantra –almost illegal not to mention here– will forever be ingrained.

To all the master students of the 'ballenbak' F218 –**Lisa**, **Laurens**, **Margriet**, **Janice**, **Christian**, **Rick**, **Sarel**, **Tijmen**, **Gerben**, **Sezer**, **Thomas**, **Douwe**, **Colin** and **Lars**– the uncountable number of shared coffees and frustrations made these ten months what they were. Keep the traditions alive (especially the horrible Christmas decorations), and to the next vrijmibo or borrel! Lisa, thank you for drawing me into this mess, I will never forget your words 'work hard, play hard'. And finally Rick and Lars, it is a shame the terrible Frans Duits tradition was never ported to the master room.

To all of **Team Diamond**, keep staying awesome! It is a shame I missed just about every possible social activity, but I heard they were great. You make an awesome work environment, and the many (way too early) lunches will be missed.

To all the **TNO** folks on the QLink project, it was definitely an experience to be thrown into such a complex project. It was inspiring to see the project evolve from frustration to well-oiled, and to see the decades of experience and expertise come together. Thanks as well for the book, I'm enjoying the read and feel smarter already!

Beyond the hard work for this thesis, it would be impossible to mention all the friends who made this time in Delft what it was, but here's an attempt to name at least a few: **Dakje**, I promise I'll hold my 21 diner one day, and I can't wait for Guatemala; **BAMB**, it was an awesome lustrum and I hope you'll forgive the late beer emails the last few months; all the **Forze** baes, I look forward to the next F1 game or random borrel; **Oelektrisch**, maybe one day I'll join another oelebar; and finally a special mention to **Mees** and **Nicky**, thank you for being there during my darkest hours.

Igolt and **Eveline**, your infinite support has made me the person I am today. I simply cannot even begin to thank you for that. And finally **Teye**, beat you to it once again, suck it! But in all seriousness, I literally would not know what to do without you.

Thank you!